공학박사 학위논문

Generation and active steering of optical beams based on nanometallic structures

금속 나노 구조물에 기반한 광학 빔의 형성과 능동 조종

2016년 8월

서울대학교 대학원

전기컴퓨터공학부

송 의 영

Abstract

Generation and active steering of optical beams based on nanometallic structures

Eui-Young Song

Department of Electrical Engineering and Computer Science

College of Engineering

Seoul National University

Generation and active control of highly collimated and non-diffractive beams based on nanometallic structures are rapidly gaining popularity in applications that require exquisite control over light concentration and emission processes. Although much effort has been devoted to developing nanoscale structure for active control of optical beams, no practical active device architecture has been established yet. Research on active control of optical beams even at the single-pixel level on the microscale or nanoscale has been rare.

In this dissertation, various optical beams (e.g. Airy beams, caustic beam, cosine-gaussian beams and plasmonic beams) are generated and steered based on nanometallic structures. Three noble methods are introduced: mechanical actuation , oblique incidence of light, and changing wavelength.

First, a novel mechanism for active directional beaming by mechanical actuation of double-sided plasmonic surface gratings is proposed. It is shown that the asymmetric mechanical actuation of optimally designed plasmonic surface gratings surrounding a subwavelength metal slit can produce a steerable off-axis beaming effect. The controllability of the beam direction provides an opportunity to develop novel active plasmonic devices and systems.

Second, plasmonic complex fields are generated with double-lined distributed nanoslit segments. As a unit cell, two facing nanoslits are used for tuning both the amplitude and the phase of excited SPPs as a function of their tilted angles. For verification of the proposed design rule, experimental demonstration of some plasmonic caustic curves and Airy plasmons is presented.

Finally, a new method to launch the finite power Airy beams based on the metasurface is presented. By tailoring the amplitude and phase of the transmitted fields from the metallic C-aperture array, the launching of Airy beams has been achieved in free space. This structure has multi-frequency characteristic which facilitates Airy beam steering because the trajectory of Airy beams is dependent on the wavelength. Experimental demonstration shows that the Airy beams can be steered by tuning wavelength very easily.

These findings facilitate the realization of a new class of active optical beam shaping for use in new optical sources and a wide range of nanoscale optical spectroscopy applications.

Keywords: Optical beams, non-diffraction beams, optical beaming, metasurface, plasmonic beams, Airy beam, Caustic beam

Student Number: 2012-30939

Contents

List of Tables

List of Figures

Chapter 1 Introduction

1.1 Overview of optical beams

In many field of optics, it is necessary to shape and control a beam or pulse of light so that it has specific properties. In particular, for applications in optical tweezers [1], microscopic imaging [2], 3D display [3], and plasmonic laser [4], it is important to have a well designed beam with specific amplitude and phase distribution. However, localized light would broaden spatially through diffraction which is a nature of electro-magnetic waves. Therefore, the generation of directional beam and non-diffraction beam is a fundamental issue in photonics. Moreover, practical active device architecture for dynamic control of these beams have been in strong demand in various fields [5]. There are various methods and applications for generation of the non-diffraction beams and directional beams. In following subsections, generation of these beams will be briefly reviewed.

1.1.1 Non-diffraction beams

Diffraction has to be considered in all forms of waves because the light expands or converges as it propagates. Diffraction is a limiting issue in many applications although one may wish to have long interaction or propagation lengths where the transverse dimensions of the light field do not expand appreciably. Non-diffraction beam is invariant with respect to diffraction

from one plane to the next. A plane wave is an example of such a field. This wave is a solution of Helmholtz equation which governs the propagation of monochromatic light. Transversal intensity shape of this solution is propagation invariant which makes it 'non-diffracting'. It turns out that plane waves are not unique in this respect and that unbounded solutions to the Maxwell equations exist which localize their energy along the optical axis more effectively than plane waves. Laser beams offer coherent and monochromatic light outputs that have low divergence over a long propagation distance. In the research area such as microscopy and sensor, however, it is necessary to have the smallest possible beam spot sizes to focus and collimate propagating light.

One possible way of finding another non-diffraction beam is to decompose any non-diffraction light field into a set of plane waves. Plane waves provide us with a basis set by which one may expand any given light field. If there are geometries of plane waves where each wave accrues exactly the same phase shift as each other, this is the case of all straight propagating "non-diffracting" beams. Such light fields appear exactly the same at any given plane in their propagation direction and are termed propagation invariant. This leads to the property of immunity to free space diffraction as the form of the superposition does not change at all on propagation. Beyond the plane wave the most popular "non-diffracting" modes are Airy beam, Bessel beam, and Mathieu beam.

In 1978, Berry and Balazs first predicted the non-spreading wave packet from the Schrödinger equation in quantum mechanics for a free particle [6]. This wave packet is a non-trivial solution of the Schrödinger equation by

exploiting the formal analogy between the free-particle Schrödinger equation and the paraxial equation of diffraction. The remarkable features of this Airy packet are non-spreading, freely accelerating, and self-healing ability. In 2007, optical version of the Airy wave packet, called Airy beams, was investigated and observed experimentally by introducing finite-energy Airy beams [7]. Although the generated beam is not ideal Airy packet, the beam still showed all the interesting characteristics of ideal Airy packet: non-diffraction, free-acceleration and self-healing. The propagation dynamics of a diffraction-free Airy beam is shown in Fig. 1.1.

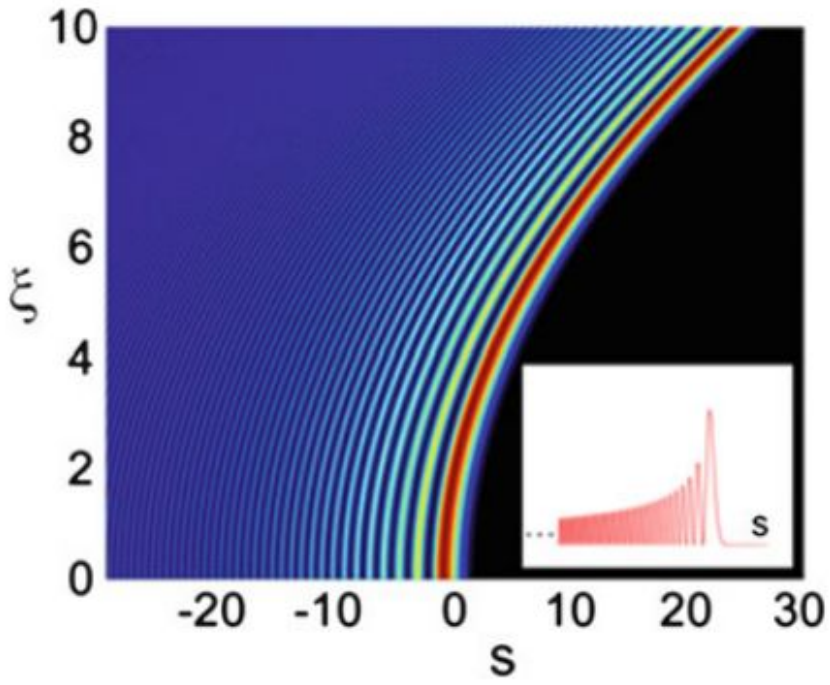

Figure 1.1 The propagation dynamics of a diffraction-free Airy beam. The corresponding input intensity of the beam is shown in the inset [7].

Second kind of non-diffraction beam is Bessel beam. The Bessel beam as a mathematical construct was first noted by Durnin [8-10]. Durnin looked at Whitaker's solutions of the Helmholtz equation and saw that particular solutions of the Bessel type were independent of the propagation direction. More important perhaps were the properties of this solution; in particular such a beam could have near diffraction limited features which did not spread. Of course the reality is a little more down to earth. A Bessel beam gets its name from the description of such a beam using a Bessel function, and this leads to a predicted cross-sectional profile of a set of concentric rings. Mathematically the Bessel beam can contain an infinite number of rings, and so over an infinite area would carry infinite power. So the conclusion must be that we cannot make a Bessel beam. What Durnin and coworkers went on to show was that one could make an approximation to a Bessel beam (a quasi-Bessel beam) experimentally which possesses the properties of the mathematical entity over a finite distance. The propagation dynamics of a diffraction-free Bessel beam is shown in Fig. 1.2.

One may also consider the "non-diffracting" Mathieu beams [12, 13]: these represent a set of closed-form expressions that are solutions of the Helmholtz equation and may be considered as elliptical generalizations of the well known Bessel beams. The propagation dynamics of a diffraction-free Mathieu beam is shown in Fig. 1.3.

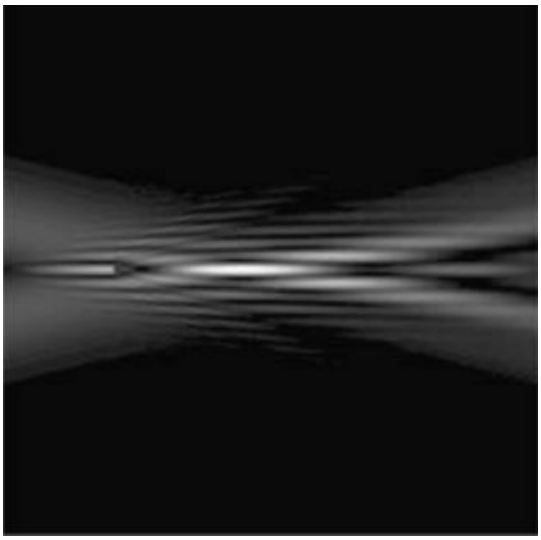

Figure 1.2 The propagation dynamics of a diffraction-free Bessel beam [11].

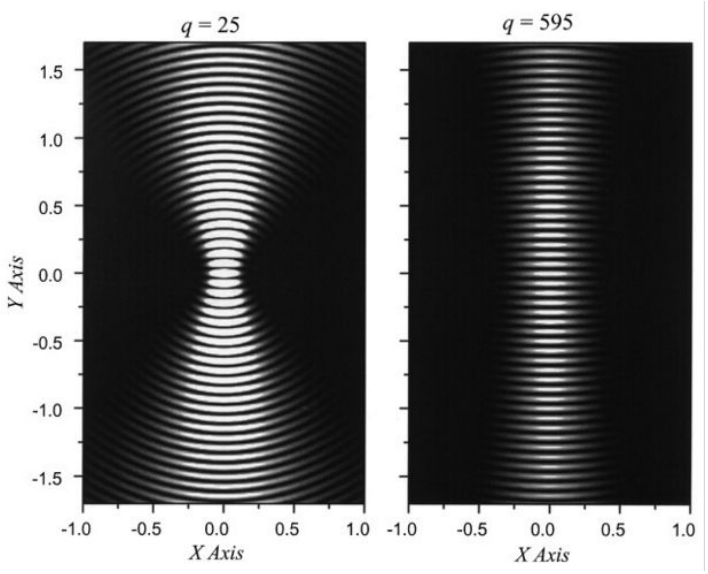

Figure 1.3 The propagation dynamics of a diffraction-free Matheiu beam [12].

1.1.2 Highly collimated beam: optical beaming

When electromagnetic waves are coupled with conduction electrons at a metal-dielectric interface, they can form a kind of surface waves, referred to as surface plasmon polaritons (SPPs) that can be concentrated at the interface in a subwavelength scale [14]. Directional beaming occurs when all re-radiated SPPs propagate in the same specific direction. Since its first implementation, various plasmonic structures (mostly subwavelength slits or holes with gratings on the emitting surfaces) have been proposed. In designing these structures, an accurate estimation of the diffraction angles of SPPs plays a key role. Fig 1.4 shows the example of directional beaming.

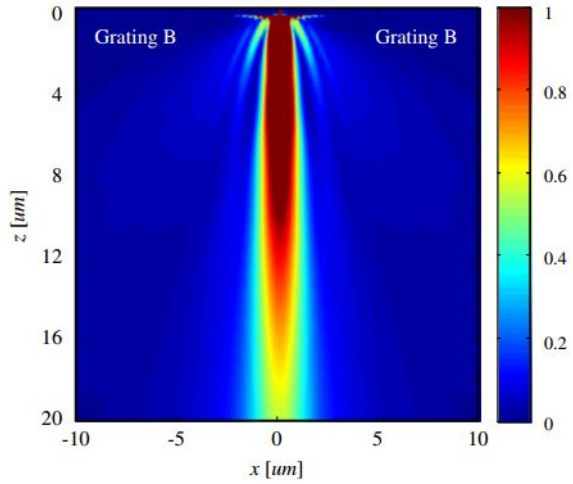

Figure 1.4 Example of directional beaming using double-sided surface gratings[14].

1.1.3 Applications of optical beams

Optical beams can be applied to many field of optics. In this subsection, some examples of the applications will be reviewed. This work is very important because the review instructs us to see the recent progress and improvement plans of generating optical beams. Specifically, we will review three instructive applications: optical manipulation, microscopic imaging, and optical antennas for fluorescent emission.

Optical manipulation has emerged as a substantial field in biological and colloidal sciences which need to manipulate micro- and nano- particles. The ability to influence the trajectories of particles is essential for observing phase transitions and initiating optical sorting. This functionality can be facilitated by using novel light fields. The micro- and nano- particles respond to the gradient and scattering forces and follow trajectories not commensurate with the flow direction. In particular, non-diffracting beams have been used to trap atoms and microscopic particles. In 2008, Jörg Baumgartl and his coworkers demonstrated the first use of the Airy light beam in optical micromanipulation [1]. Based on the characteristic intensity pattern, the beam drags particles into the main intensity maximum, which guides particles. This phenomenon can be applied to remove the particles and cells from a section of a sample chamber which is named 'optically mediated particle clearing', which can be applied to the colloidal and biological sciences. In Fig. 1.5, the strategy for optically mediated particle clearing is shown.

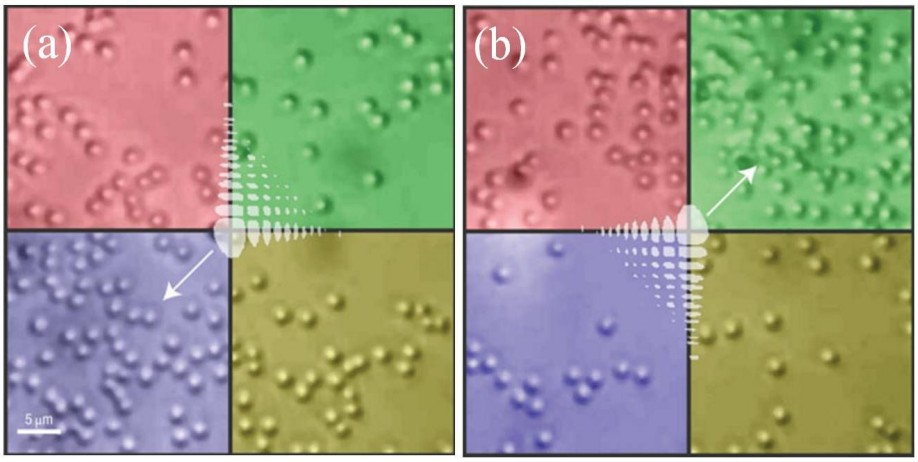

Figure 1.5 (a) Micrographs of the sample after colloids were exposed to the Airy beam, incident from below, for 2 min (b) the micrograph shown in (a), the Airy beam was rotated by 180° [1].

Optical beams can be also applied to the microscope [2, 15]. Traditional light-sheet microscopy uses Gaussian light sheet whose rapid divergence restricts the field of view that provides innate subcellualr resolution. In contrast, Tom Vettenburg and his coworkers showed that Airy beam has relatively long beam waist which yields high contrast and resolution up to a tenfold larger FOV [15]. In addition, Airy beam shows better contrast than Bessel beam because Airy beam's characteristic asymmetric excitation pattern results in all fluorescence contributing positively to the contrast. In Fig 1.6, comparison of three non-diffraction beams for microscope is shown. The controlled reduction of scattering or beam spreading would enable a new illumination concept for light microscopes.

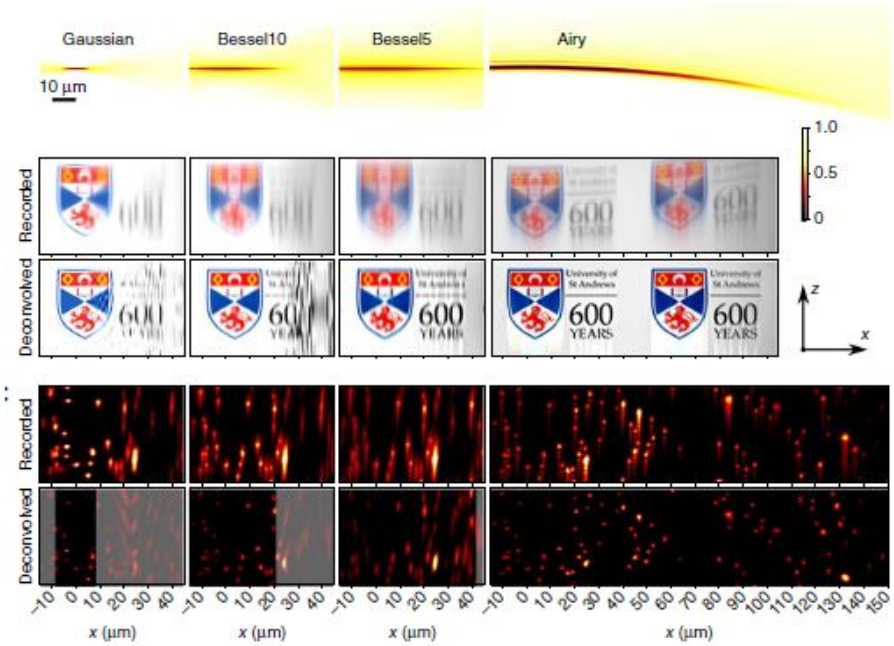

Figure 1.6 Comparison of light-sheet illuminations with various beam types: Gaussian beam, Bessel beam, and Airy beam [15].

Optical antenna for fluorescent emission is important application in bio-optics [16, 17]. Nanometallic optical antennas are rapidly gaining popularity in applications that require exquisite control over light concentration and emission processes. Spontaneous emission of fluorescent molecules or quantum dots is radiated along all directions when emitters are diluted in a liquid solution, which severely limits the amount of collected light. Besides, the emission direction does not carry any useful information and cannot be used to sort different molecules. To go beyond these limits, optical antennas have been recently introduced as conceptual tools to control the radiation properties for nanoemitters fixed on a substrate.

1.2 Objective and scope of this dissertation

In previous subsections, I briefly reviewed the generation of various optical beams and their applications. Especially, generation of non-diffraction beams and optical beaming was introduced. Most of non-diffraction beams were generated by the light with THz or GHz regime using spatial light modulator (SLM). However, micro-size pixels of the SLM or liquid crystal restrict the design of non-diffraction beams because these require bulky optical system and limit the application for small-scale or integrated beam-shaping devices. Nonlinear generation and manipulation of non-diffraction beams also suffers from long crystal length for making sufficient nonlinear effect.

Therefore, the motivation of this dissertation is to propose novel methods of generation and control of optical beams which are applicable to the integrated optical circuit. To achieve this purpose, the proposed devices have to have three characteristics: compactness, broadband, and active control. Of course, proposed devices in this dissertation did not have all the three characteristics. However, these devices have more improved design methods then previous works. For example, generation of plasmonic non-diffraction beams is more compact than other methods. Generation of optical non-diffraction beams have more compact and broadband characteristics.

The subjects which will be discussed are briefly categorized in Table 1.1.

Table 1.1 Categorized subjects which will be discussed in this dissertation.

	Plasmonic beam shaping	**Optical non-diffraction beam in free space**	**Optical directional beaming**
Method	1. Slit patterns 2. Gratings 3. Metasurface	1. SLM modulation 2. Liquid Crystal 3. Metasurface	1. Modulating fields from SPPs by using surface gratings
Application	Plamonic multiplexer, Particle manipulation,	Microscopy, Particle manipulation, Second harmonic generation	Sensing, Optical lithography
Requested improvement for integration	Complex modulation, Active control	Complex modulation, Compact, broadband, active control	Active control

The objective of this dissertation is to propose new methods of generation and control of optical beams which can be applicable to integrated optical device. For this purpose, two types of optical beams are proposed: one is optical beams propagating in free space, the other is SPP beams propagating on the metal film. These beams would be generated and actively controlled using various methods.

In Chapter 2, a novel mechanism for active directional beaming by mechanical actuation of double-sided plasmonic surface gratings is proposed. It is shown that the asymmetric mechanical actuation of optimally designed plasmonic surface gratings surrounding a subwavelength metal slit can produce a steerable off-axis beaming effect. The controllability of the beam direction provides an opportunity to develop novel active plasmonic devices and systems.

In Chapter 3, a novel method for generating a plasmonic complex field propagating with arbitrary curvatures by using double-lined distributed nanoslits would be proposed. Since the surface plasmon polariton (SPP) has received a great deal of attention because of its capability of guiding light within the subwavelength scale, finding methods for arbitrary SPP field generation has been a significant issue in the area of integrated optics. To achieve such a goal, it will be necessary to generate a plasmonic complex field. As a unit cell, two facing nanoslits are used for tuning both the amplitude and the phase of excited SPPs as a function of their tilted angles. For verification of the proposed design rule, I experimentally demonstrated some plasmonic caustic curves and Airy plasmons. In addition, steering method of plasmonic caustic beams would be discussed.

In Chapter 4, a novel method for generating and steering of Airy beams based on linear optical metasurface is proposed. To accomplish this, I used split ring resonators (SRRs) aperture arrays in which each SRR has its own tilted angle. The amplitude and phase of Airy beam profile can be substituted as unit cells and tailored by tuning only the tilted angles of the SRRs. Furthermore, the proposed metasurface has a broadband characteristic in

optical regime. This facilitates steering of Airy beams by tuning the wavelength of incident light because the trajectory of Airy beams is a parabolic curve whose curvature is dependent on the wavelength. In comparison to previous approaches for generating and controlling Airy beams, my designing method shows many important merits – ultrathin subwavelength pixel size for compact system, broadband characteristic, simple design strategy, and linear optical devices which means that this method is more energy efficient than nonlinear metasurface method. To the best of our knowledge, it is the first realization of Airy beams having both broadband and compact (main lobe: ~ 2μm) characteristics.

Finally concluding remarks to this dissertation are presented in Chapter 5. The objective and scope of this dissertation are depicted in Fig. 1.7.

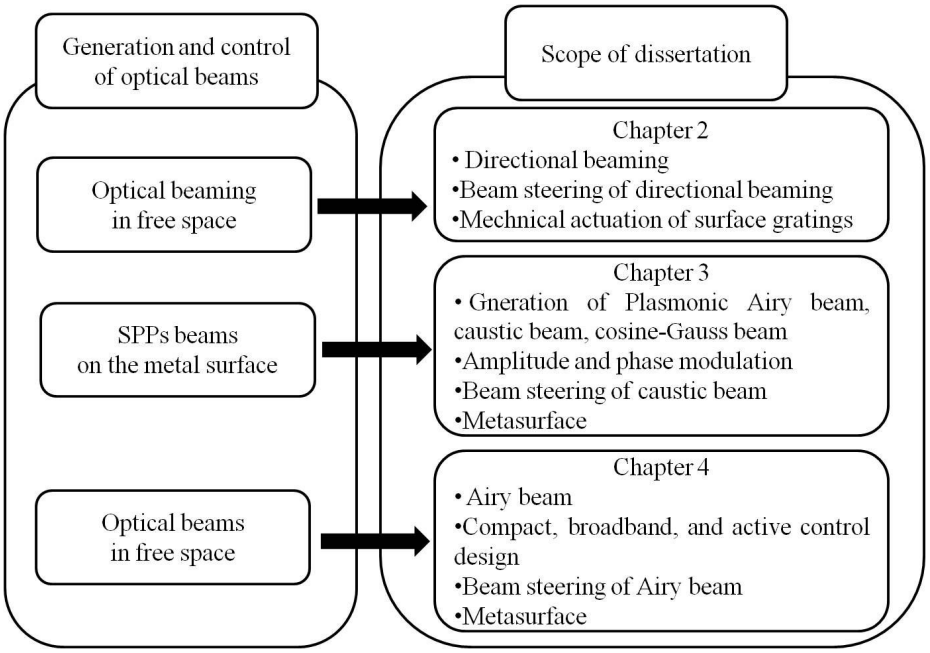

Figure 1.7 Objective and scope of this dissertation

Chapter 2 Active directional beaming by mechanical actuation of double-sided plasmonic surface gratings

2.1 Introduction

Micro-scale or nano-scale directional beaming devices that can be actively controlled have been in strong demand in various fields [18]. In the field of three-dimensional (3D) displays, the generation of directional images with directional differentiation is a fundamental issue. Device-level implementation of this functionality is extremely difficult at present [19]. The development of high-speed dynamic directional light devices could produce time-sequential light field distribution to generate 3D images in space. It would also provide novel functionality for applications in photonic integrated circuits, optical communications, optical computing, optical sensing, optical manipulation of molecule, and 3D displays. Although much effort has been devoted to developing micro-scale static directional beaming structures [20-22], no practical active device architecture for dynamic beaming has been established yet. Research on dynamic directional beaming even at the single-pixel level on the micro-scale or nano-scale has been rare [23].

Recently, nano-electro-mechanical systems (NEMS) technology has

been emerging as one of the most powerful technologies for realizing nano-scale active photonic devices. Active metamaterials [24] and spatial light modulators [25] were fabricated based on NEMS technology.

Considering the potential application of NEMS technology to photonics, we propose a novel mechanism for a nano-scale active directional beaming device based on the mechanical actuation of double-sided plasmonic surface gratings.

2.2 Basic concept of active directional beaming based on mechanical actuation of double-sided plasmonic surface gratings

2.2.1 Schematic diagram and basic concept of operation

I show that the asymmetrically lifted double-sided plasmonic surface grating structure generates a directional beaming effect, as shown in Fig. 2.1. Fig. 2.1 illustrates the basic mechanism of directional beaming. Two diffracted beams with the same direction of radiation, and formed by diffraction of the leftward and rightward surface plasmon (SP) waves are spatially superposed by the surface gratings. This results in collimated directional beaming. The grating period, the dielectric thickness, and the thin metal (Ag) layer thickness are denoted as p, t_d and t_m, respectively. The air-gaps of the left and right surface gratings are denoted as t_L and $t_{R,}$, respectively. The left and right dielectric gratings have the same permittivity but different lifting air-gaps, t_L and t_R.

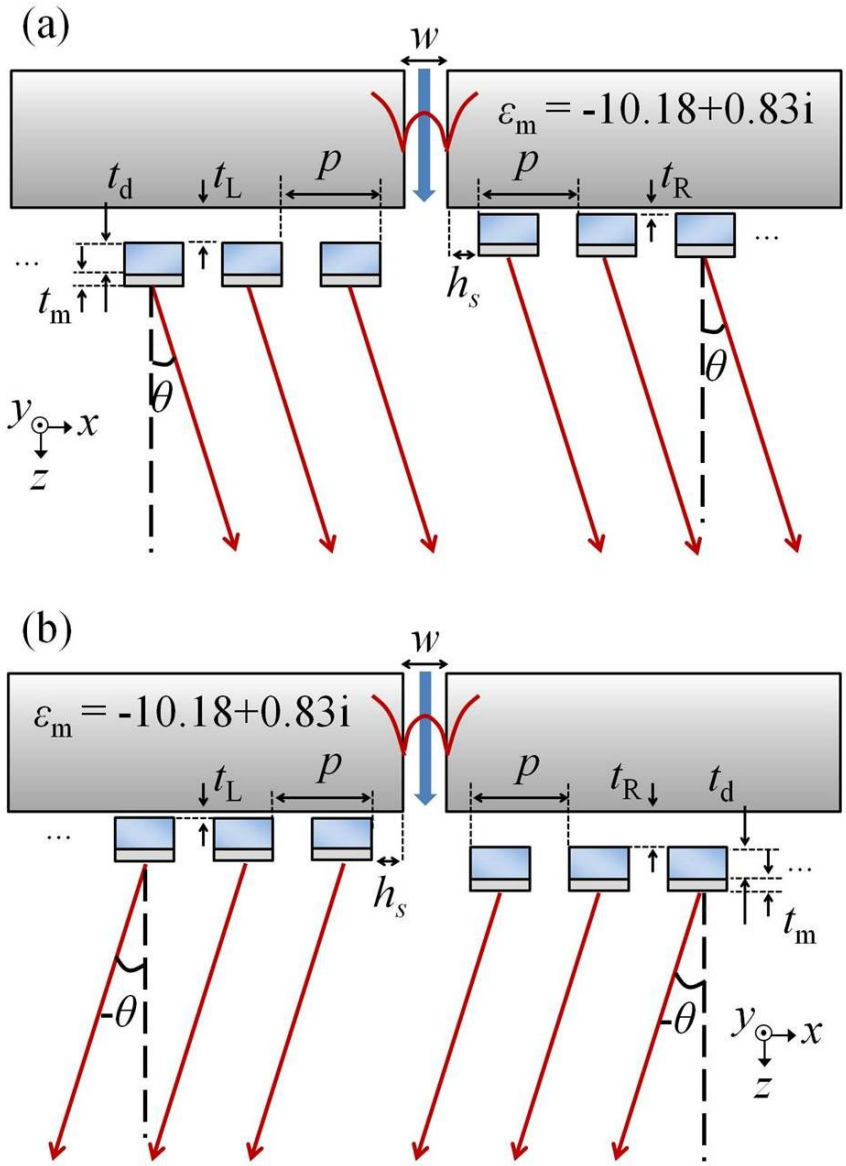

Figure 2.1 Directional beaming effects by the subwavelength metal slit with double-sided plasmonic surface gratings with period p, the left and right air-gaps of t_L and t_R, and the offset of h_s in cases of (a) $t_L > t_R$ and (b) $t_L < t_R$.

The directionality of the beam is determined by the air-gap

configuration of the double-sided surface grating, (t_L, t_R). The effective refractive index of the grating material can be tuned by the air-gap between the floating surface grating and the metal substrate interacting with the SP waves. Actually, the effective refractive index of the grating material is the degree of freedom providing controllability of the beaming direction [26]. In ref. [26], it was shown that the radiation angle increases monotonically with the refractive indices of the double-sided gratings. The direction of the diffracted beam can be controlled by lifting the surface gratings to balance the effective refractive indices of the left- and right-gratings. The right-directional and left-directional beaming effects with respect to the air-gap configuration of the surface gratings (t_L, t_R) are illustrated in Figs. 2.1(a) and 2.1(b), respectively. Analytically, this can be explained by the grating equation as follow [26],

$$k_{x,rad} = \mathrm{Re}\{n_{SPP}^{R}\}k_0 - \frac{2\pi}{p} = \mathrm{Re}\{-n_{SPP}^{L}\}k_0 + \frac{2\pi}{p}, \qquad (2.1)$$

where $k_{x,rad}$ is re-radiated wave along the transvers (x) direction, the superscripts R and L indicate that they correspond to the right- and left-side gratings, respectively. If n_{spp} is identified as the effective index under effective medium theory, it can be rewritten as [26],

$$n_{spp} = [(1-f)n_b^2 + fn_g^2]^{\frac{1}{2}}, \qquad (2.2)$$

where, f is fill factor of gratings, n_b is effective index of the SPP mode in the bare region, and n_g is the effective index of the SPP mode in the ridge region. By Eqs. (2.1) and (2.2), It can be concluded that the variation of air-gap

changes the radiation angle.

2.2.2 Single sided surface gratings for various grating permittivity

Before discussing double-sided plasmonic surface gratings, it would be instructive to summarize ref. [23], briefly. Fig. 2.2 shows the single sided grating structure. This structure is single-side version of Fig 2.1 which has equal parameters. The observation of the single-sided grating structure would provide basic information about the radiation angle with refractive indices of the single-sided gratings. To simulate this configuration, the optimal design parameters of the proposed structure have been found for an operating wavelength of 532nm with the COMSOL Multiphysics simulator. The permittivity value of metal (Ag) is -10.18+0.83i at this wavelength and that of the grating dielectric material is set to 2.8. A parametric optimization process was used to decide the optimal structural parameters. The periods of right gratings (p=390 nm), fill factor (f= 0.45), offset (h_s=20 nm), dielectric thickness (t_d=80 nm), and thin silver coating thickness (t_m=20 nm) are set to the same values for the two gratings. The slit width w is 100 nm.

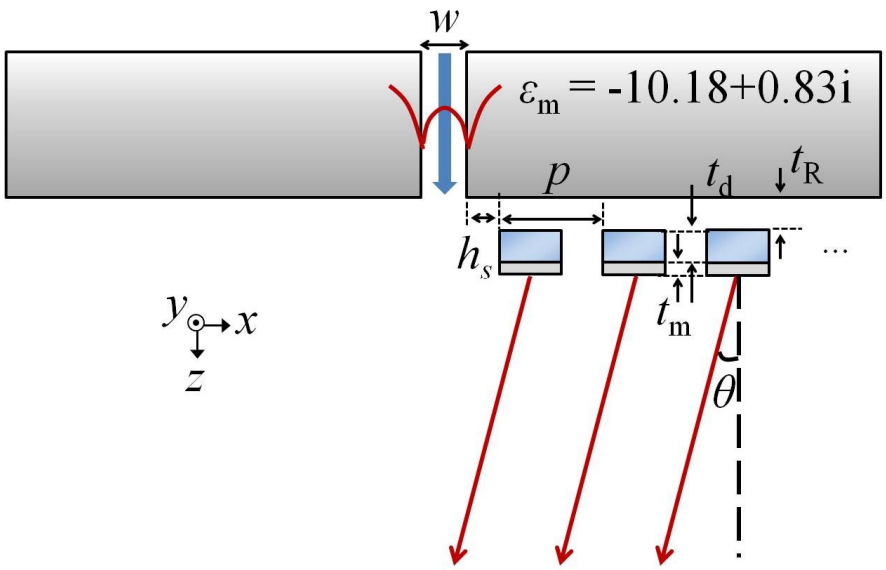

Figure 2.2 Schematic diagram of single-sided plasmonic surface grating structure.

The electric field intensity distributions for the air-gap 0 nm, 10 nm, 20 nm, 30 nm, and 40 nm are shown in Fig 2.3. Main finding in this simulation is that the variation in the air-gap value of the proposed metal-dielectric composite grating directly changes the beam radiation angle. By superposition, therefore, the direction of the diffracted beam can be controlled by lifting the surface gratings to balance the effective refractive indices of the left- and right-gratings in the double-sided plasmonic surface gratings configuration.

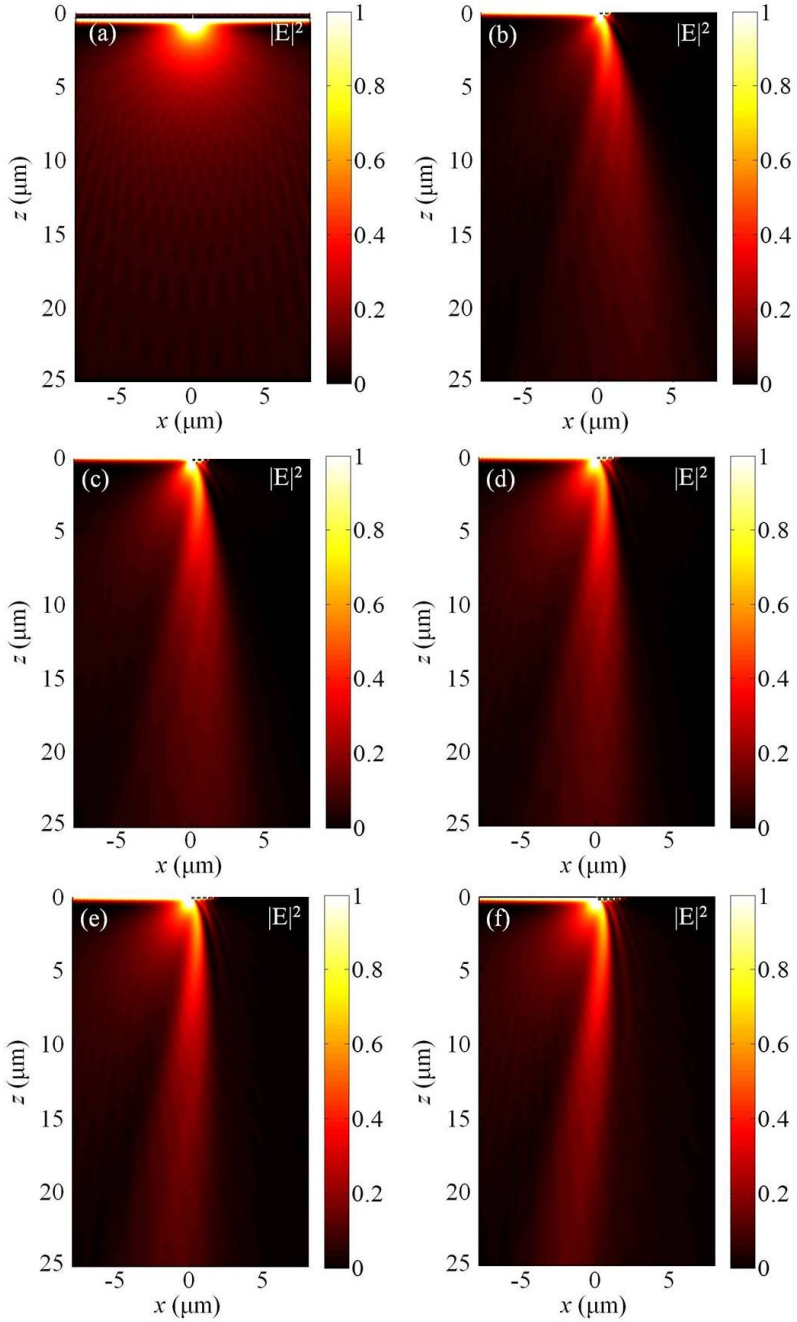

Figure 2.3 The electric field intensity distributions for the air-gap (b) 0 nm, (c) 10 nm, (d) 20 nm, (e) 30 nm, and (f) 40 nm. (a) is bare case for reference.

2.3 Analysis of surface gratings: waveguide view

The floating grating in the ridge region can be modeled by the metal/air/dielectric/silver/air layer [27] as shown in Fig. 2.4.

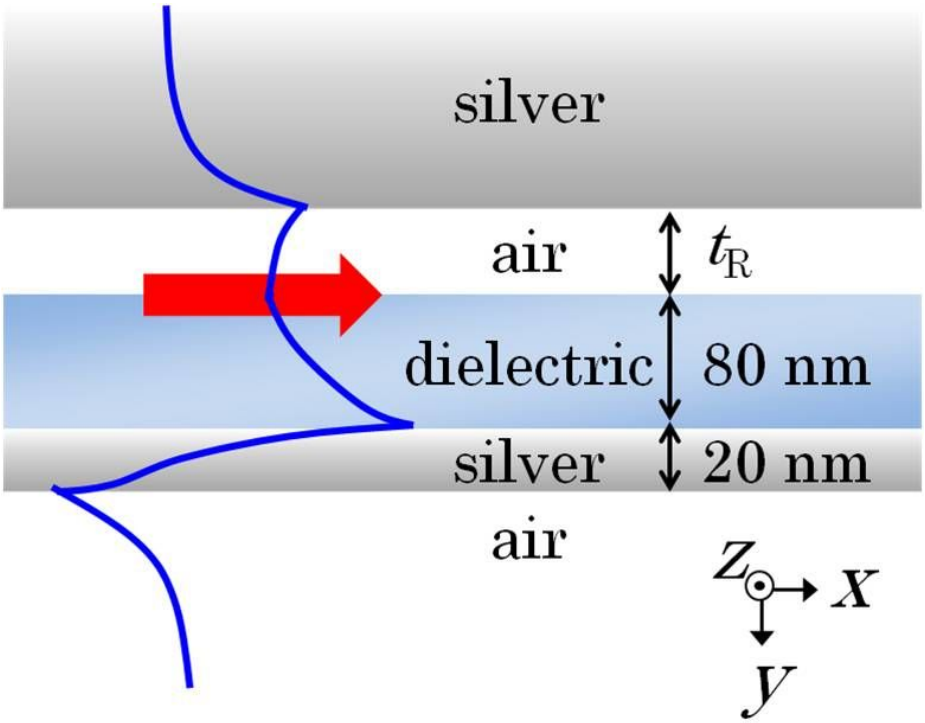

Figure 2.4 Schematic diagram of metal-air-dieletric-metal-air layers and SP mode propagating along the +*x*-direction

The effective refractive indices of the SP modes interacting with the floating grating are analyzed in Fig. 2.5. For this analysis, the thicknesses of the dielectric and the thin silver layers, t_d and t_m are set to 80nm and 20nm, respectively. The wavelength is 532 nm at which the permittivity of silver is -10.18+0.83i. The permittivity of dielectric is selected to be 2.8.

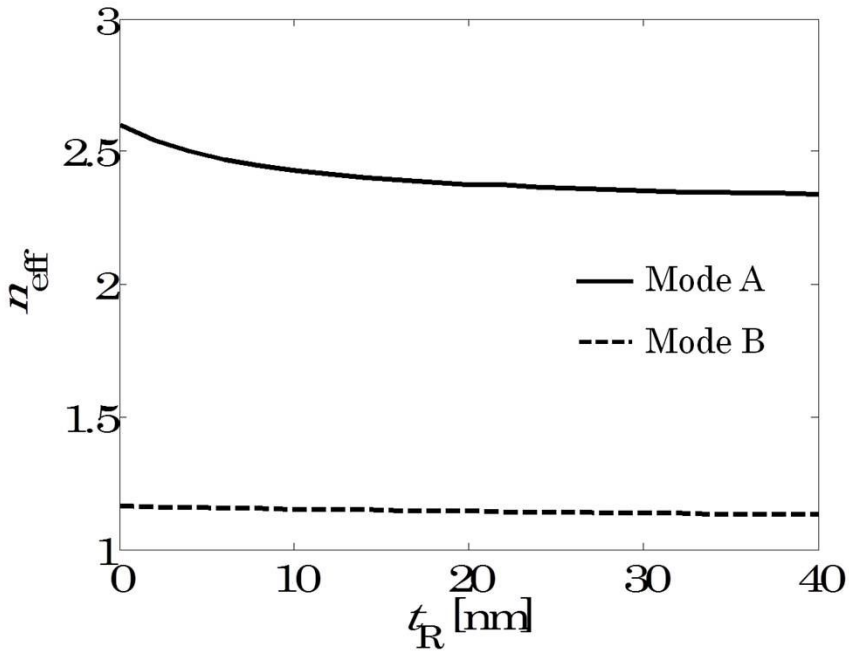

Figure 2.5 Profiles of effective indices of metal/air/dielectric/metal/air layers. There exist two SP modes(mode A and B) in the multilayer structure.

There exists two modes: mode A and mode B. The effective refractive index of the mode A is a monotonically decreasing function with respect to t_R in the range of 0 nm to 40 nm. This variation in effective refractive index by the air-gap implies that t_L and t_R in Fig. 2.1 are monotonically increasing and decreasing functions of the beaming angle θ, respectively. For the air-gap configurations with $t_L > t_R$ and $t_L < t_R$, it can be expected that the radiation angles would be $\theta > 0$(deg) and $\theta < 0$(deg), respectively. For the second SP mode (mode B), an almost constant effective refractive index (n_{eff} =1.2) is extracted. However, Mode B would generate noise field. To analyze these two modes, the magnetic field profiles of two

modes at t_R =20 nm are shown in Fig. 2.6. The mode A propagates mainly through the lossless dielectric and thin silver layers, having a long propagation length, while the mode B is tightly confined near the metal substrate decaying fast and thus the contribution of the mode B to the beaming is negligible. Consequently, the mode A with a longer propagation length contributes to the formation of the beaming field dominantly.

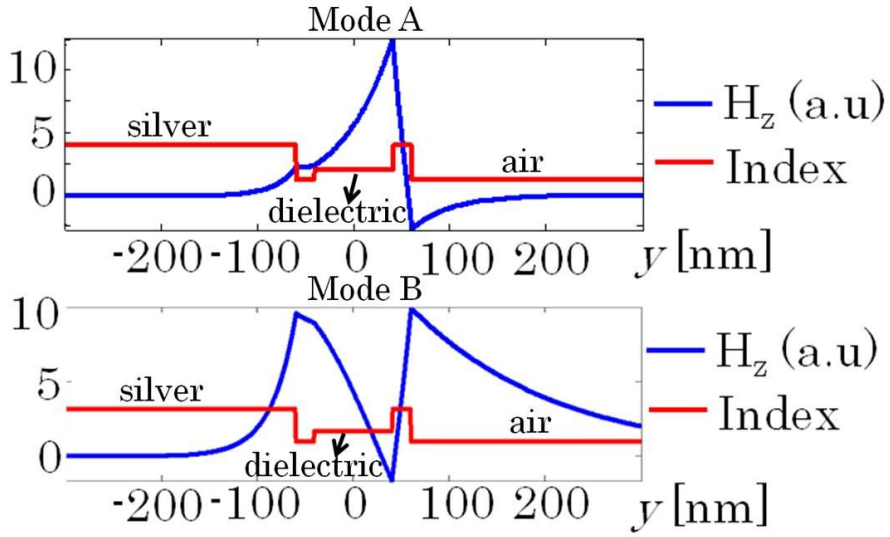

Figure 2.6 The magnetic field of the two modes and refractive index profiles of the multilayer structure.

2.4 Demonstration of active directional beaming

The diffraction field distribution generated by subwavelength metal slits with no gratings is visualized in Fig. 2.7. In Figs. 2.7(b)-(d), directional off-axis beaming by asymmetrically lifting double-sided gratings is demonstrated. As shown in these figures, the radiation angles in the cases of (t_L,t_R)=(40 nm, 0 nm), (20 nm 20 nm), and (0 nm, 40 nm) are obtained as θ=5.4(deg), θ=0(deg), and θ=-5.4(deg), respectively.

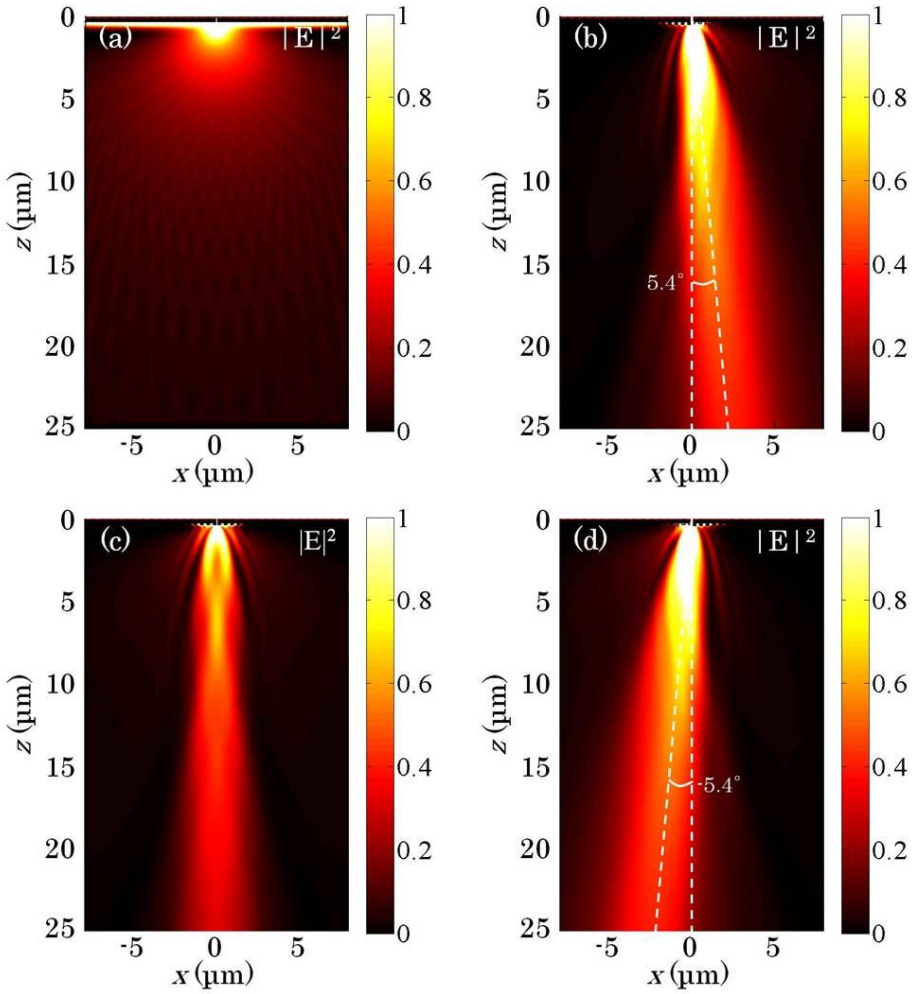

Figure 2.7 (a) Diffraction field distributions generated by the subwavelength metal slits with no grating. (b)-(c) Diffraction field distributions with air-gap configurations of the double-sided surface gratings for the left- and right-gratings of (b) (t_L, t_R)=(40 nm,0 nm), (c) (t_L, t_R)=(20 nm, 20 nm), and (d) (t_L, t_R)=(0 nm, 40 nm).

2.5 Design strategy of active directional beaming

As mentioned in previous section, these directional beamings are the result of superposition of two beams diffracted by the lifted left- and right-gratings. For more detail, the grating air-gap configuration for the angle of radiation is calculated as a function of the radiation angle θ in Fig. 2.8. In Fig. 2.8, $t_L(t_R)$ is calculated by measuring the angle of diffraction-field distributions generated by the metal slits with the single right-side(left-side) surface gratings without left-side(right-side) surface gratings for t_R. The air-gap variation is constrained in the range of 0 nm to 40 nm. The figure shows that t_L and t_R are nonlinear monotonically increasing and decreasing functions of θ, respectively. For any specific radiation angle θ in the range of -5.4(deg) to +5.4(deg), an appropriate air-gap configuration pair (t_L, t_R) can be obtained.

When the air gap is greater than 40 nm, the surface grating does not interact with the evanescent field tail of the SP wave propagating on the metal slit surface. The second SP mode presented in Fig. 2.5 is immune to the air gap variation, which implies that the diffraction of the second SP mode does not change with the air gap variations. The beaming effect shown in Fig. 2.7 is mainly ascribed to the diffraction of the first SP mode whose effective refractive index is sensitive to the air gap variation. In Fig. 2.7, the diffraction field components of the first and second SP modes are actually mixed. However, in the proposed structure, the coupling power of the slit to the interactive first SP mode is estimated to be greater than that to the noninteractive second SP mode, and thus the dynamic directional beaming operation is confirmed as demonstrated in Fig. 2.7.

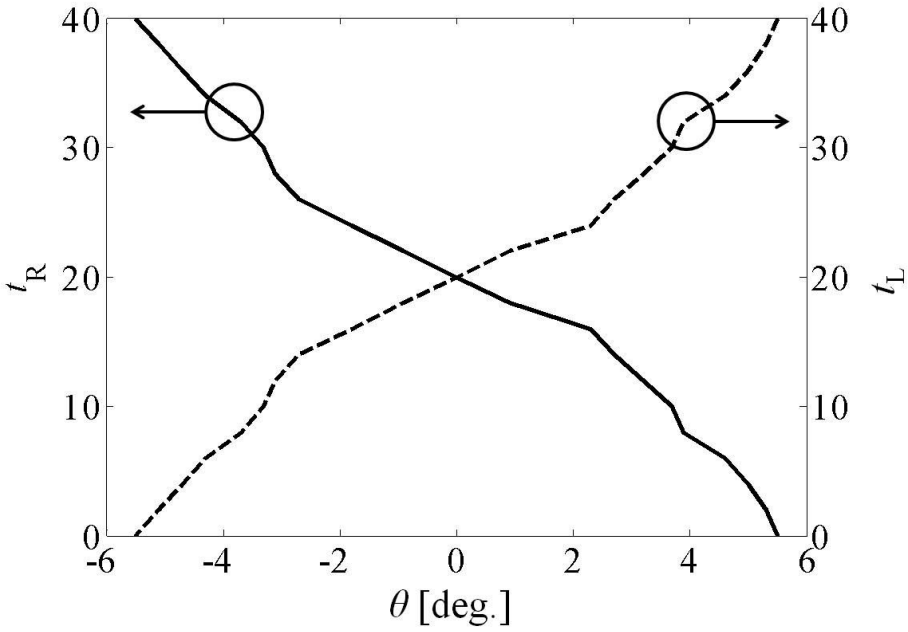

Figure 2.8 Air-gap value t_L and t_R as a function of the radiation angle θ of the diffracted beaming field.

2.6 Experimental suggestion

In practice, the control of lifting the grating structure can be implemented using NEMS technology. An array of nano-scale clamped-clamped beams with metal electrodes at each corner is a good example [28]. A voltage will be applied between the beam and the electrode to control t_L and t_R. The central portion of the structure whose air gap thickness is adjusted electrically, sustains the surface grating structure and will be exposed to light. Calculations show that about 13 V is needed to actuate TiN clamped-clamped beams whose length, width and thickness are 10 μm, 0.1 μm and 30 nm, respectively when t_L and t_R are 50 nm [28]. The air-gap distance from 0nm to 50nm can be linearly controlled by adjusting the bias voltage within the 13V range.

The beam steering angle can be widened by an additional micro lens system. According to the law of space bandwidth product conservation, if the image of the slit is imaged into a smaller image, the beam tilting angle can be increased proportionally to the magnification rate. Although the issue of increasing the dynamic range of the beam tilting angle is a continual focus in our research, the initial conditions of the small dynamic steering range are a cornerstone for the advanced engineering of active plasmonic beam steering devices.

2.7 Conclusion

In conclusion, a novel mechanism for active directional beaming by mechanical actuation of double-sided plasmonic surface gratings was proposed. Two diffracted beams with the same direction of radiation, and formed by diffraction of the leftward and rightward surface plasmon waves are spatially superposed by the surface gratings. This results in collimated directional beaming. It was shown that the radiation angle increases monotonically with the refractive indices of the double-sided gratings. The direction of the diffracted beam can be controlled by lifting the surface gratings to balance the effective refractive indices of the left- and right-gratings. Finally, it was shown that the asymmetric mechanical actuation of optimally designed plasmonic surface gratings surrounding a subwavelength metal slit can produce a steerable off-axis beaming effect. The controllability of the beam direction will provide an opportunity to develop novel active plasmonic devices and systems. The proposed directional beaming architecture based on NEMS would be further extended to various active plasmonics applications. An experimental implementation of the proposed structure is being prepared and will be reported in the near future.

Chapter 3 Plasmonic complex field generation and steering with double-lined distributed nanoslit segments

3.1 Introduction

In the field of nanophotonics, there has been a pursuit for methods to manipulate optical surface waves within the subwavelength scale. One of possible ways to achieve highly-confined optical wave beyond the diffraction limit is using surface plasmon polaritons (SPPs), which are electromagnetic surface waves formed by collective oscillations of photons and electrons on the surface of conductors [29]. Therefore, the spatial control of both of the amplitude and phase of SPP wave has been considered as a very important issue. Such complex modulation of SPP field makes possible to realize the perfect generation of an arbitrary SPP wavefront profile, and such a capability would lead to the innovation of technologies in many fields of optical science and engineering such as optical trapping [30, 31], routing of SPP energy along particular trajectories [32-34], next-generation optical holography [35, 36], and biosensing [37, 38].

While spatial light modulators (SLMs) are the most popular choice for

complex field modulation in free space, these kinds of devices do not exist for SPPs. For this reason, various methods for manipulating wavefront of SPP were proposed in recent years. Plasmonic vortices introducing geometrical phase shift by shaping curved slits [39-41], binary modulated grating using holographic method for beam shaping [42-44], graded index methods for modifying optical path [45-47], and manipulating SPP propagation using periodic scatterer [48-50] are the examples of these efforts. However, to the best of my knowledge, most of these methods are phase-only type or only applicable to special cases [34, 51]. Although generation of plasmonic Airy beam has been demonstrated through complex modulation [33], the work needs bulky system implementation with SLM.

On the other hand, recently, metasurface has been emerging as one of the most powerful methods for controlling amplitude and phase profile of light in free space [52-54]. A metasurface is often defined as an artificially designed two-dimensional structure that is composed of arrays of subwavelength-size unit cells. The unit cells of metasurfaces interact with the incident light that results in changes in the optical properties of the incident light. Given the fact that metasurfaces can be employed to manipulate light in free space, these design principles were also applied for manipulating the phase of SPPs by using nanoslit arrays. The unit-cells of metasurfaces interact with the incident light which causes the changes of optical properties of incident light. Very recently, with the merit of metasurfaces to manipulate light in free space, these design principles were also applied for manipulating phase of SPPs by using nanoslit arrays. It was shown that columns of slanted nanoslits provide polarization-controlled tunable directional coupling which

facilitates both bidirectional and unidirectional launching of SPPs [55]. Single or double arrays of nanoslits with a specific tilted angle distribution were also proposed, which can switch the direction and length of focus by tuning polarization [56]. Similar concepts were applied to plasmonic vortex lens consisting of circularly distributed nanoslits [57, 58]. Moreover, a method for polarization-multiplexing of SPP phase profiles has been proposed [59]. However, these schemes are still limited to phase control of SPPs. The method for arbitrary generation of complex SPP field is not demonstrated yet.

In this chapter, a novel method to generate plasmonic complex field propagating with arbitrary curvatures is proposed. Fig. 3.1 shows the schematic diagram of proposed structure. To accomplish the goal, I used double-lined distributed nanoslit arrays in which each nanoslit has its own tilted angle. It is shown that both of the amplitude and phase of generated SPP can be independently controlled by tuning the tilted angles of nanoslits. Therefore, with the backside illumination of left circularly polarized (LCP) light or right circularly polarized (RCP) light, the proposed double-lined distributed nanoslits can generate arbitrary complex SPP field. Furthermore, steering method of generated beam will be proposed.

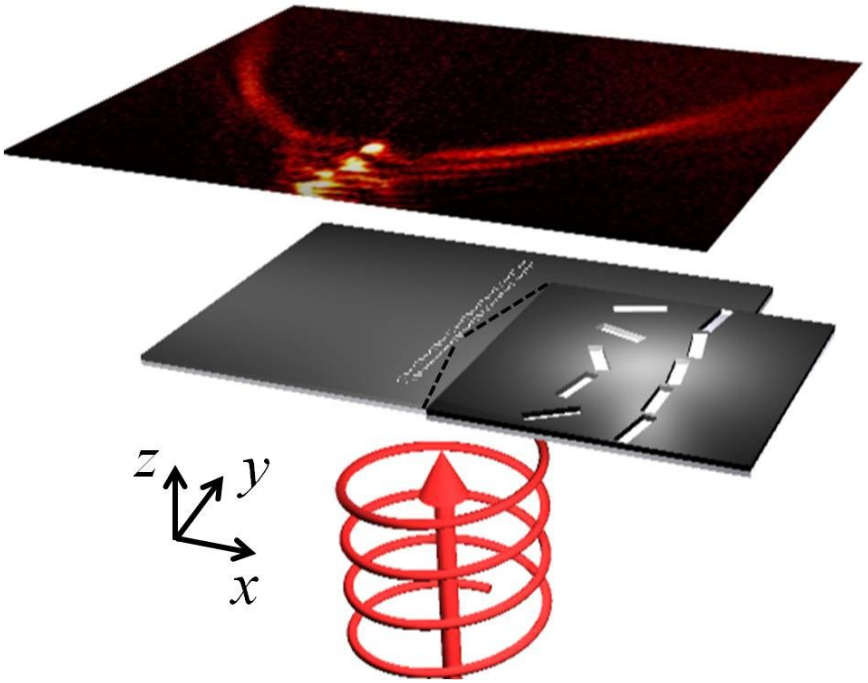

Figure 3.1 Schematic diagrams of the proposed complex SPP field-generation.

3.2 Characteristics of single lined nanoslit array

Although SPP excitation characteristics from single-lined nanoslit array with a constant tilted angle was already analyzed in [56], I would like to briefly mention it again for clear understanding of the proposed structure. If the period of slit is shorter than the effective wavelength of the SPP (λ_{SPP}), plane-wave SPP field is generated on the normal illumination of circularly polarized light. Because it is possible to model each nanoslit as a dipole source that lies on the metal surface directing normal to the longer axis of the nanoslit, the superposition of dipole sources generates quasi-planewave SPP field. The amplitude (A) and phase (Φ) profile of launched SPP propagating in +x-direction can be approximated as follows [56]:

$$A(\theta) = A_0 \left|\cos(\theta)\right|, \tag{3.1}$$

$$\Phi(\theta) = \pm\left(\theta - \pi u\left(\theta - \frac{\pi}{2}\right)\right). \tag{3.2}$$

The plus and minus signs of Eq. (3.2) correspond to the cases of LCP and RCP incidence respectively, and the function u indicates the unit step function. In Eqs. (3.1) and (3.2), there is only one degree of freedom (θ) for controlling; therefore it is not possible to fully implement the complex field. To independently modulate the amplitude and phase of SPP wave, at least two degrees of freedom in designing complex field generation device are needed, which will be introduced in the next section. In Fig. 3.2(a), single lined nanoslit segments with a constant tilted angle θ are shown. Figs. 3.2(b)

and 3.2(c) are the plotted results of Eqs. (3.1) and (3.2), respectively.

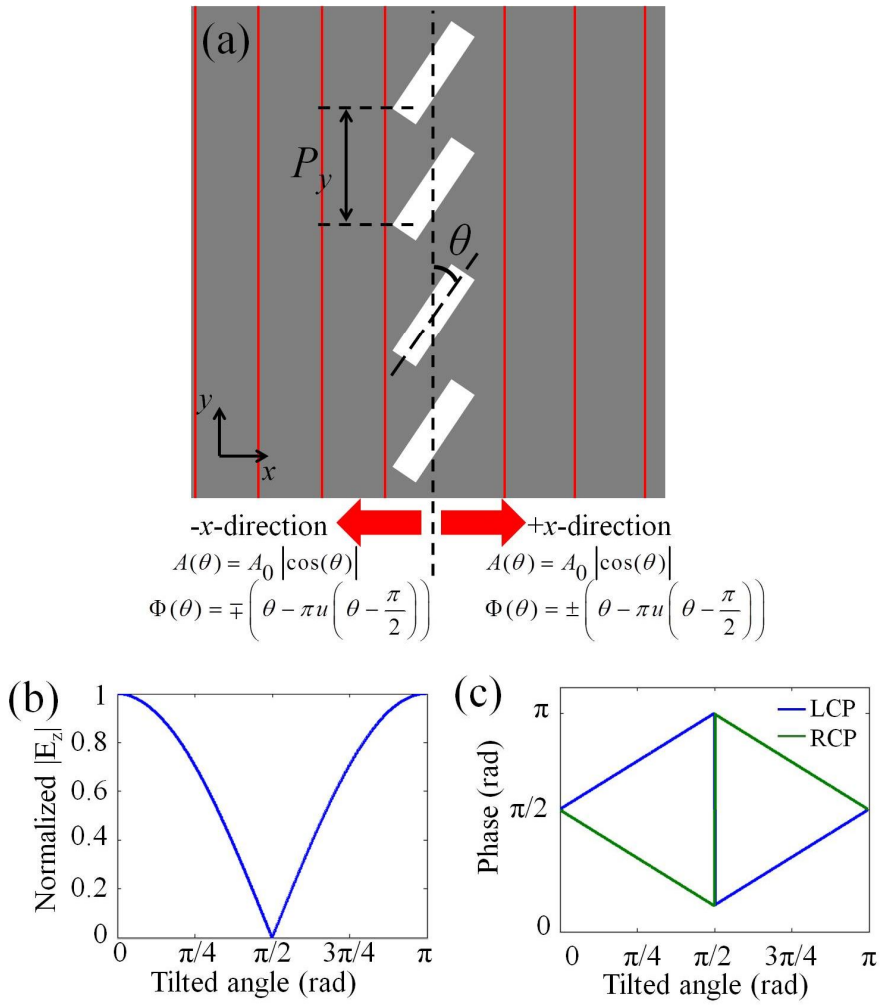

Figure 3.2 (a) Schematic diagram of single lined nanoslit segments with constant tilted angle θ. The period of slit segments is P_y. Red line represent propagation of SPP. (b) Amplitude profile of SPP as a function of tilted angle. (c) Phase profile of SPP as a function of tilted angle.

3.3 Characteristics of double lined nanoslit array

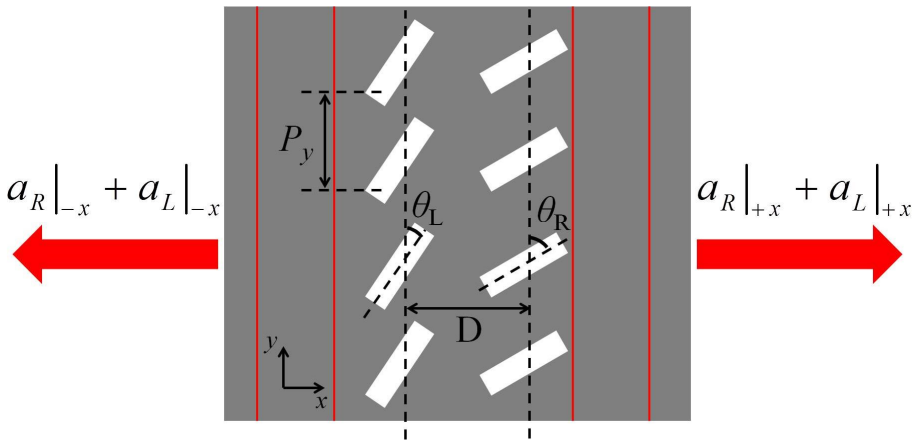

Figure 3.3 Schematic diagram of double-lined distributed nanoslits with constant tilted angles of θ_L and θ_R. The period of slit segments is P_y. Red lines represent propagation of SPP.

From now, I propose double-lined distributed nanoslits which have two degrees of freedom (θ_L and θ_R) as shown in Fig. 3.3. Throughout this paper, the distance between two lines is given by $D=\lambda_{SPP}/2$. Therefore phase difference between left- and right-side lines caused by geometrical distance is always π in our configuration. The range of generated plasmonic complex field can be calculated by using Eqs. (3.1) and (3.2). These two equations can be rewritten in the compact form as $A(\theta)e^{j\Phi(\theta)} = \cos(\theta)e^{\pm j\theta}$. If I define the complex amplitude of SPP field propagating along $+x$-direction generated by right(left)-side array of nanoslits as a_R (a_L), the interference of these two fields can be expressed as

$$a_R\big|_{+x} + a_L\big|_{+x} = \frac{1}{2}\left(1 - e^{\pm j2(\theta_L - \theta_R)}\right)e^{\pm j2\theta_R}, \tag{3.3}$$

where plus and minus signs of Eq. (3.3) correspond to the cases of LCP and RCP, respectively. According to Eq. (3.3), the amplitude of SPP can be modeled as angular difference of two nanoslits ($\Delta = \theta_L - \theta_R$), whereas the phase is controlled by the offset rotation angle. Equation Eq. (3.3) was plotted in Fig. 3.4(a) for LCP incidence and in Fig. 3.4(b) for RCP incidence where the θ_R is changed from 0 to $3\pi/4$. If the θ_R is changed from 0 to π, the unit circle of complex plane can be fully filled which means full range of complex field generation. This facilitates arbitrary complex field generation if I consider the two slits located at the same *y*-axis as a unit cell. It is noteworthy that SPP field propagating along –*x*-direction can also be expressed as

$$a_R\big|_{-x} + a_L\big|_{-x} = -\frac{1}{2}\left(1 - e^{\pm j2(\theta_L - \theta_R)}\right)e^{\pm j2\theta_R}, \tag{3.4}$$

which has equal magnitude and opposite sign with Eq. (3.3).

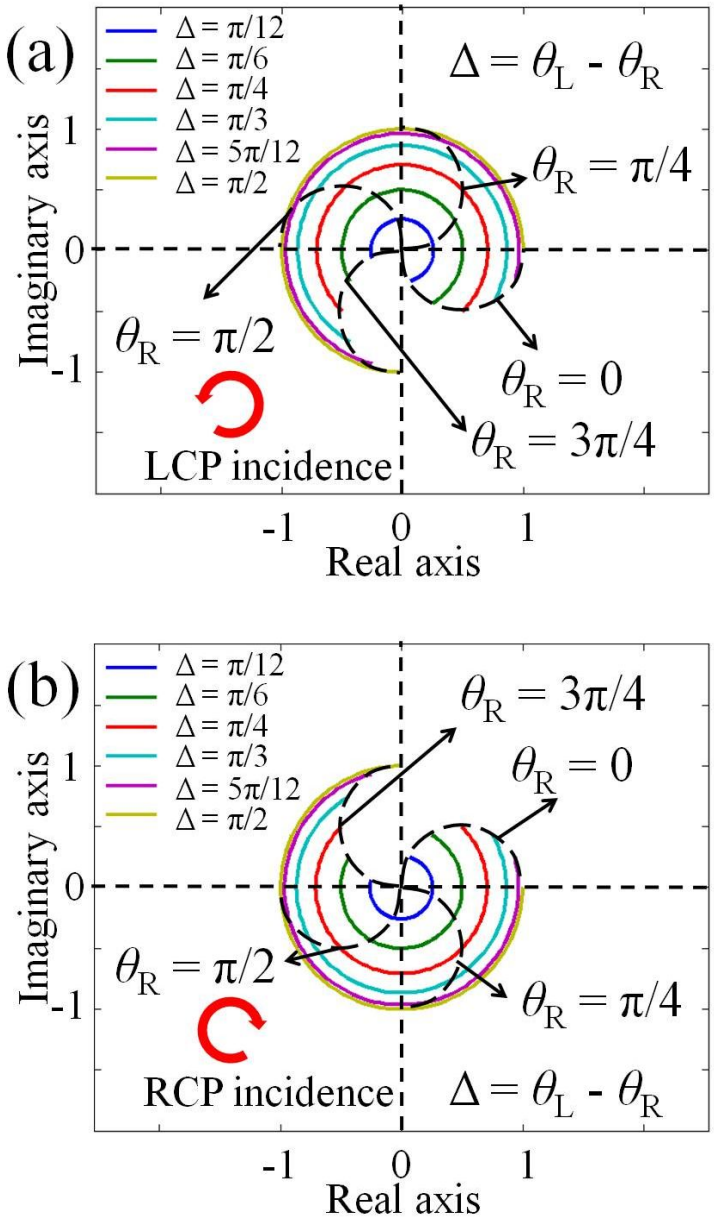

Figure 3.4 For (a) LCP incidence and (b) RCP incidence, the range of complex field modulation is plotted when θ_R is changed from 0 to 3π/4.

3.4 Design of plasmonic complex field generation

I will describe the workflow of the proposed method. I initially set the desired plasmonic complex field profile (such as caustics or Airy beam profile) to be generated. Because the SPP sources are excited from the array of discrete nanoslits, it is necessary to substitute the complex field profile with unit cell. However, there are various points to be considered in determining the unit cell period. First of all, unit cell period must be shorter than the operating wavelength to avoid unwanted interference of each source. It has been shown that such unwanted interference generates multiple beams [36]. On the other hand, the lower limit of the unit cell period is determined by the dimension of the nanoslit to avoid the attachment of neighboring two nanoslits. Two factors should be considered in determining the dimension of nanoslits: one is the desired power for generating SPPs, and the other is the resolution limit in fabrication.

In the subwavelength scale, in general, larger slit dimensions guarantee a stronger excitation of SPPs; therefore the proposed structure may have a high efficiency for larger slit dimensions. On the other hand, smaller slit dimensions ensure a shorter unit cell period which guarantees a high resolution. However, the lower limit of slit dimensions is restricted by the desired power of the generated SPPs. Therefore, it should be noted that there is a trade-off relation between coupling efficiency and unit cell resolution of the proposed structure. Moreover, the aspect ratio of the rectangular nanoslit should be carefully designed because a nanoslit with a sufficiently high aspect ratio can only maintain the high polarization sensitivity of SPP excitation characteristics.

After determining the appropriate dimension of the nanoslit and the unit cell period with the abovementioned criteria, θ_L and θ_R are determined by using Fig. 3.2(b) or 3.2(c) according to the type of circular polarization. Finally, I obtained the appropriate shape of the nanoslit array for plasmonic complex field generation. As long as the restricted slit size is realistic in fabrication, it is possible to generate an arbitrary plasmonic complex field with the proposed workflow. Summarized strategy for generating arbitrary plasmonic complex field is described in Fig. 3.5 as flow chart.

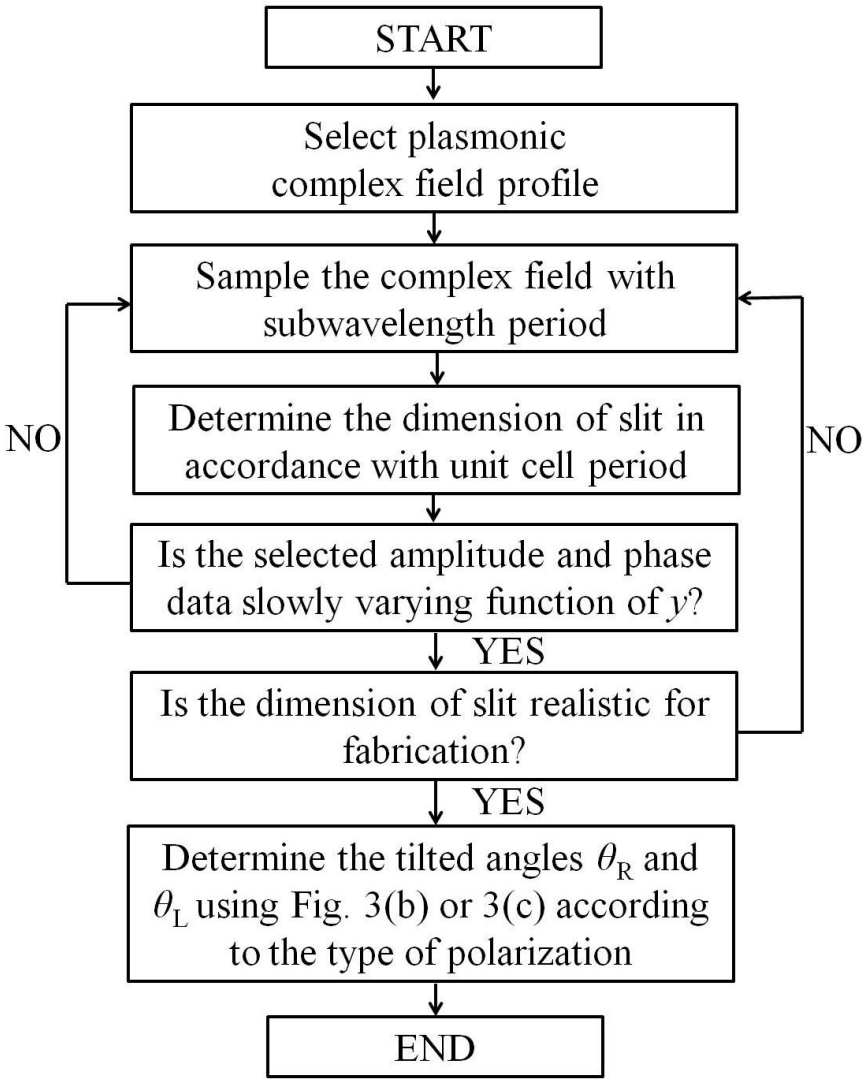

Figure 3.5 Flow chart of the design of plasmonic complex field generation.

3.5 Phase-only example: plasmonic caustic beams

3.5.1 Design of plasmonic caustic beams

In order to verify the abovementioned method, I needed to generate an SPP curve profile via caustics. The generation of an arbitrary convex wave via caustics is a well-established method as evidenced by literature references [60]. Fig. 3.6 shows the geometrical construction of a generating phase profile from the properties of an arbitrary desired caustic.

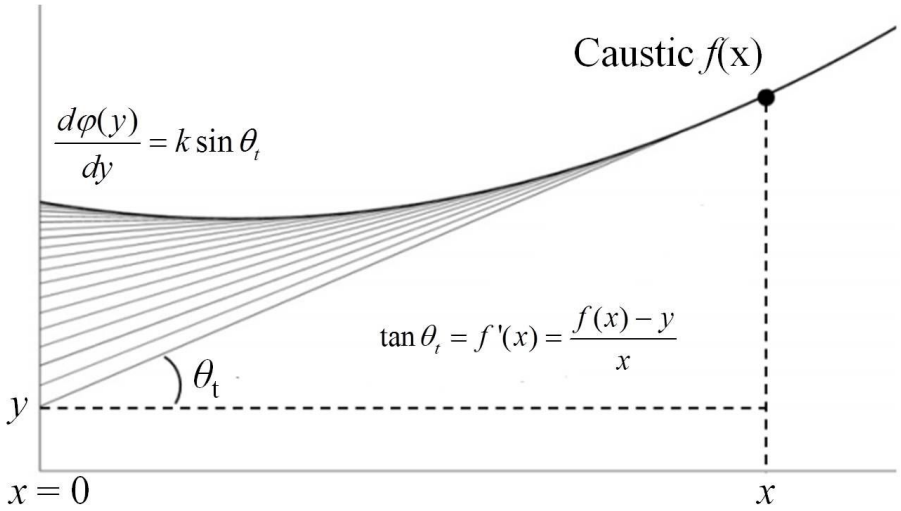

Figure 3.6 Geometrical construction of a generating phase profile from the properties of an arbitrary desired caustic [60].

If the desired analytical curve is $y = f(x)$, the corresponding spatial phase function $\varphi(y)$ at the line $x = 0$ can be calculated. The caustic curve $f(x)$ can be generated by the family of virtual geometrical tangent rays drawn by connecting each point in $y = f(x)$ with the corresponding point in $x = 0$. If the tangent of the slope is defined by θ_t, the relation between the spatial phase function $\varphi(y)$ at the line $x = 0$ and caustic curve $y = f(x)$ is expressed as [60]

$$\frac{d\varphi(y)}{dy} = k_{SPP} \sin\theta_t = \frac{k_{SPP} f(x)}{\sqrt{1+[f'(x)]^2}}, \tag{3.5}$$

where k_{SPP} is the wave number of the SPP mode. By using Eq. (3.5), $\varphi(y)$ can be calculated from $f(x)$. In our double-lined nanoslit array configuration, I set the location of the right-line nanoslit array as the reference line $x = 0$.

3.5.2 Design of double-lined nanoslits for plasmonic caustic beams

In this section, three analytical curves: $y_1 = a_1x^{1.5}$, $y_2 = a_2x^2$, and $y_3 = a_3x^{2.5}$ where $a_1 = 5.0 \times 10^{-2}$, $a_2 = 1.7 \times 10^{-2}$, and $a_3 = 4.3 \times 10^{-3}$ (in micrometer units), respectively, are generated. Using Eq. (3.5), the spatial phase function $\varphi(y)$ at the line $x = 0$ can be obtained. The amplitude profiles of these caustic curves are constant along y. Therefore, I only need to substitute the phase profile $\varphi(y)$ as unit cells. The phase profiles $\varphi(y)$ of the three curves and the locations of unit cells are shown in Fig. 3.7.

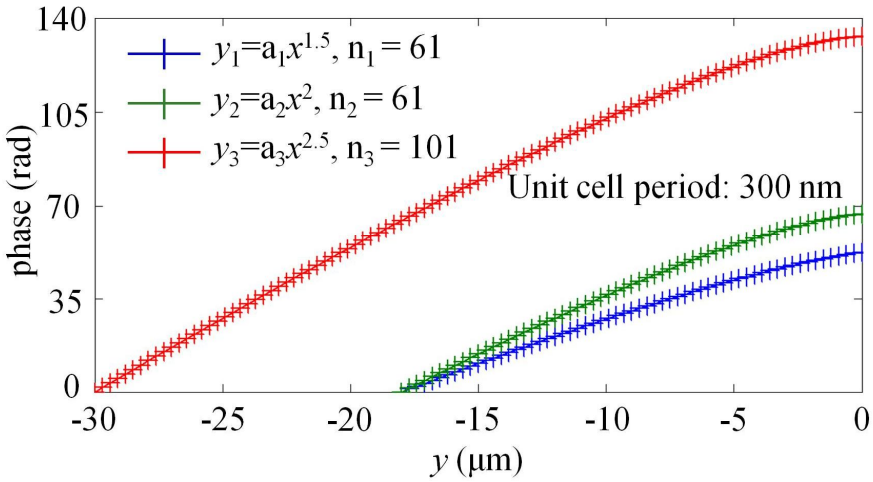

Figure 3.7 The phase profiles $\varphi(y)$ and locations of unit cells for $y_1 = a_1x^{1.5}$, $y_2 = a_2x^2$, and $y_3 = a_3x^{2.5}$. locations of unit cells are marked as '+'.

The location range of unit cells is from $y = -18$ μm to $y = 0$ μm for curves y_1 and y_2. For curve y_3, the location range is from $y = -30$ μm to $y = 0$ μm. These ranges are identical to each of the total length of the nanoslit array in the numerical simulations and experimental results. The number of each unit cell is $n_1 = 61$, $n_2 = 61$, and $n_3 = 101$ for curves $y_1 = a_1x^{1.5}$, $y_2 = a_2x^2$, and y_3

$= a_3 x^{2.5}$, respectively. The aspect ratio of slit (hight : width) dimensions have to be at least 3:1 to guarantee dipole radiation of SPPs. Hence, the period of sampling is 300 nm over all curves, and a slit dimension of 260 nm × 80 nm is used. The coupling efficiency is defined as the power of an integrated SPP at x = 3 μm divided by the total incident power passing through the opened area of the double-lined nanoslit array. The efficiency of coupling from free-space to the SPPs wave for a 260 nm × 80 nm slit dimension is calculated to be ~7%. In this section, I selected the polarization as LCP. Based on a table of the relation between a complex field and the tilted angle shown in Fig. 3.4(a), I determined appropriate tilted angles, θ_L and θ_R along the y-axis. Because the intended caustic curves need only phase modulation, I selected $\theta_L - \theta_R = \pi/2$ which guarantees the maximum power of the generated SPP. This condition corresponds to the largest circle in Fig. 3.4(a). In this unit circle, appropriate θ_L and θ_R corresponding to the phase of the designed field can be found.

3.5.3 Experimental setup

To prove the aforementioned design process is valid, I provide the experimental results with numerical simulations. For sample fabrication, the Ag layer with the thickness of 200 nm was evaporated on a fused silica wafer (MUHAN, MHS-1800). Then each slit patterns were inscribed on the Ag layer by using the focused ion beam (FIB) (FEI, Helios 650). Fig. 3.8 shows the FE-SEM images of fabricated sample for curve $y_2 = a_2x^2$.

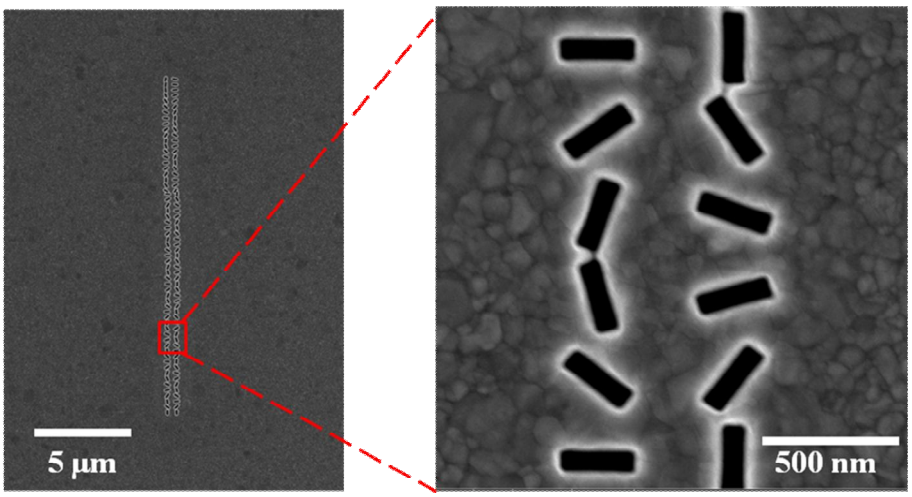

Figure 3.8 FE-SEM images of fabricated sample for $y_2 = a_2x^2$.

Then, the sample was illuminated from the bottom by the laser with the free space wavelength of 980 nm and the SPP field intensity distribution was measured by the near-field scanning optical microscope (NSOM) (Nanonics, Multiview 4000). I scanned a region of 33 μm × 33 μm at once (the maximum limit of our system) divided into 128 × 128 pixels with a duration time of 64 ms for each pixel. The experimental setup is shown in Fig. 3.9.

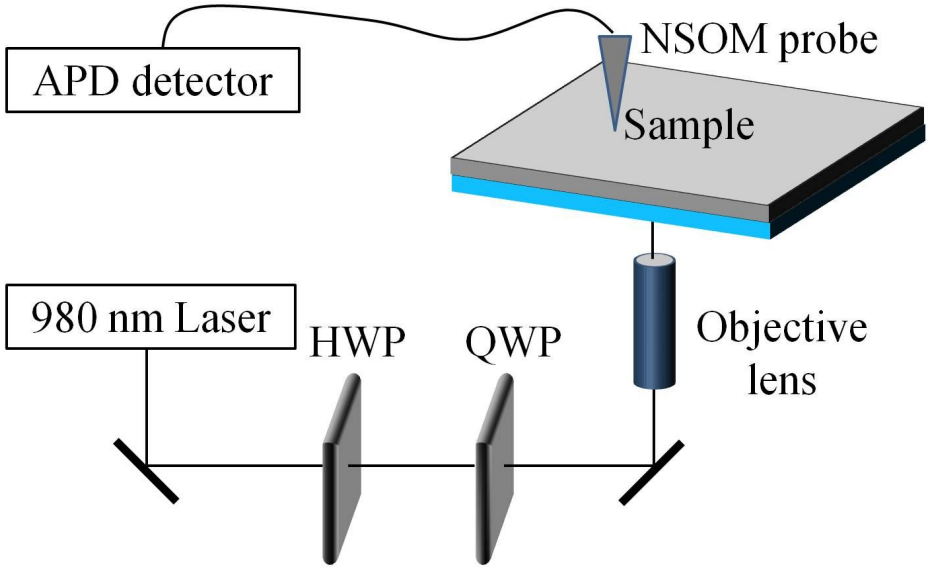

Figure 3.9 Experimental setup for near-field scanning of proposed structure. The laser source with the free space wavelength of 980 nm illuminates the bottom of sample with the circular polarization.

3.5.4 Simulation and experiment result

To simulate the intensity distribution of the generated plasmonic complex field, I employed a finite difference time domain (FDTD) analysis. The experimental results and the numerical simulations for the three curves are presented in Figs. 3.10, 3.11, and 3.12. Due to the large size of generated caustics beam (more than 33 μm in *x*-direction), each NSOM image shown in the figures is a merged image of two NSOM measurement results. Simulation results of the three curves are in good agreement with blue dashed curves which are the target curves $y = f(x)$. In addition, the symmetrical shape of the generated field intensity from the double-lined nanoslit array can be confirmed analytically, as shown in Eqs. (3.3) and (3.4). Small deviations from the blue dashed curves in Figs. 3.11(a) and 3.12(a) are evident. I concluded that this small mismatch originates from the finite length of double-lined nanoslit array. This restricts the range of the SPP curves which exactly follow the blue dashed curves.

Experimental results for the three curves also show some deviation from the blue dashed lines, showing a slightly asymmetric shape of the generated field intensity. I believe that such asymmetry occurs because the incident light is not strictly normal to the sample. The finite numerical aperture of the objective lens in the experimental setup might also play a role which causes the intensity of the incident light and the incidence angle to be non-uniform. These asymmetric deviations can be reduced by improving the overall alignment of the experiment setup.

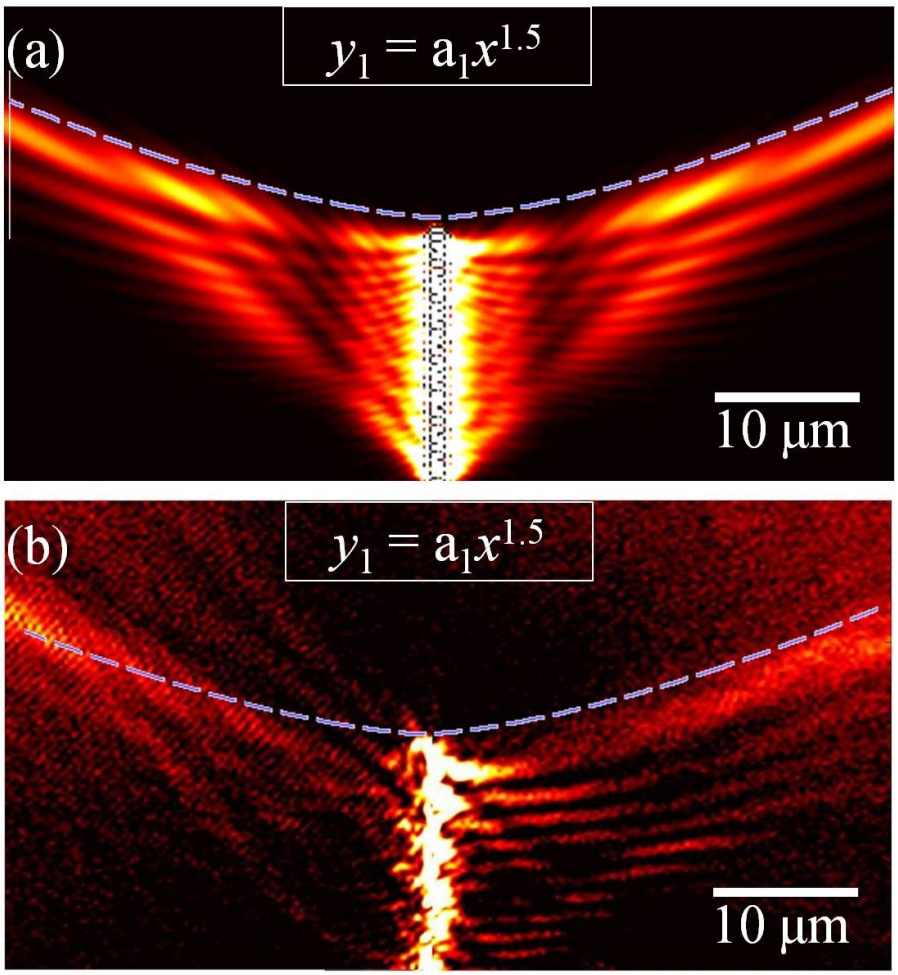

Figure 3.10 Numerical simulations and experimental results for analytical caustics curves $y_1 = a_1 x^{1.5}$: (a) simulation and (b) NSOM image.

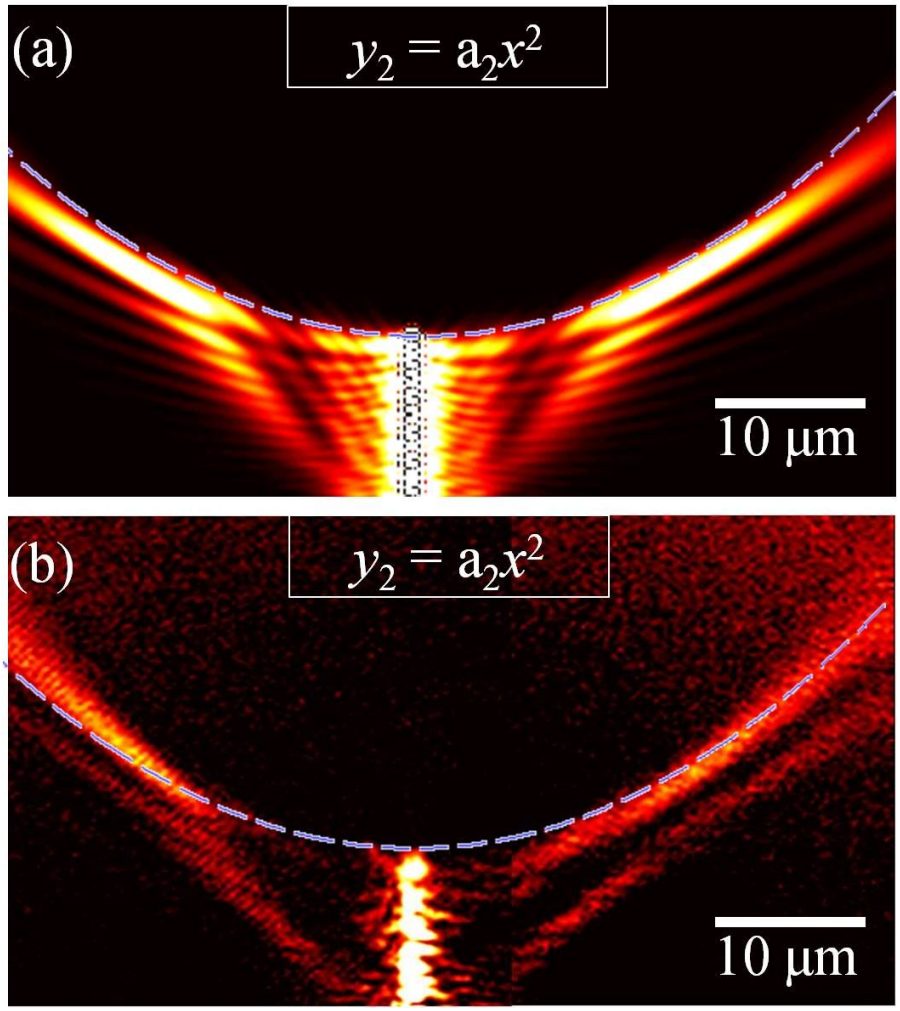

Figure 3.11 Numerical simulations and experimental results for analytical caustics curves $y_2 = a_2x^2$: (a) simulation and (b) NSOM image.

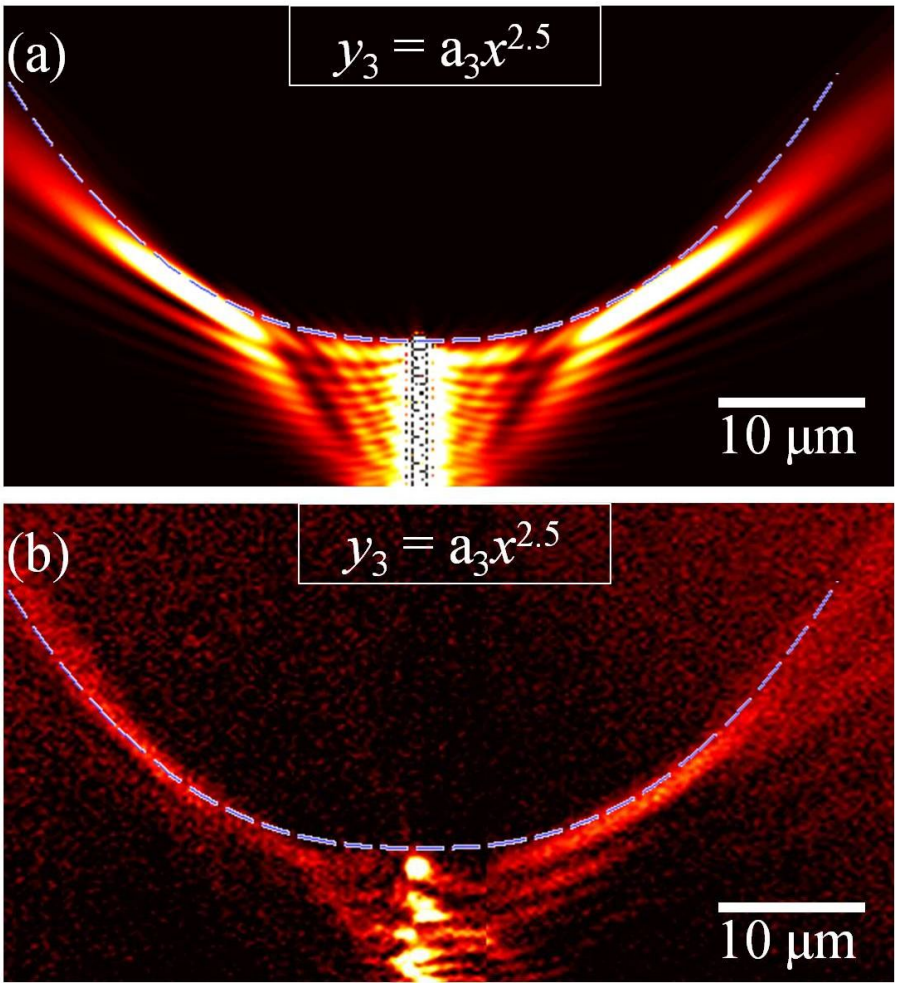

Figure 3.12 Numerical simulations and experimental results for analytical caustics curves $y_3 = a_3 x^3$: (a) simulation and (b) NSOM image.

3.6 Amplitude-only example: cosine-Gauss plasmonic beam

Cosine-Gauss beam (CGB) is a surface wave which does not diffract while it propagates in a straight line [61]. The field profile of the CGB can be expressed as

$$f(y) = \cos(k_{SPP} \sin\theta\, y) \exp\left(-\frac{y^2}{w_0^2}\right), \tag{2.6}$$

where w_0 is the beam waist, θ is a geometrical constant of the proposed structure, and k_{SPP} is the wavenumber of the SPP mode. I note that the field profile of the CGB at the excitation line does not have phase variance. Therefore, CGB represents a good example of amplitude-only plasmonic beam shaping. Following the same procedure as previous sections, I designed the tilted angles of double-lined nanoslit arrays. The constant of CGB is chosen as $\theta = 5^\circ$, $w_0 = 20$ μm with the free space wavelength $\lambda_0 =$ 980 nm. The sampling range is from $y = -42$ μm to $y = 42$ μm. The number of unit cells is 281 and the period of sampling is 300 nm. The amplitude profile of cosine-Gauss beam and the locations of unit cells are shown in Fig. 3.13.

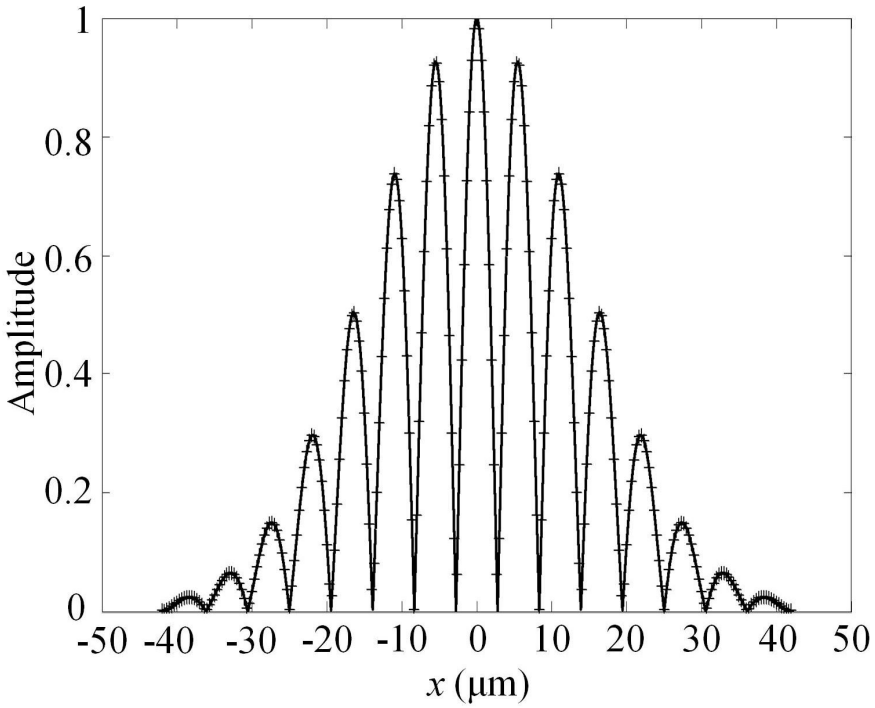

Figure 3.13 The amplitude profile and its sampling locations for cosine-Gauss plasmonic beam. Locations of unit cells are marked as '+'.

To simulate the intensity distribution of CGB, I employed the Green dyadic method. This method regards each slit as a dipole source which has been well validated in previous studies [56]. A simulation result of the intensity distribution is shown in Fig. 3.14.

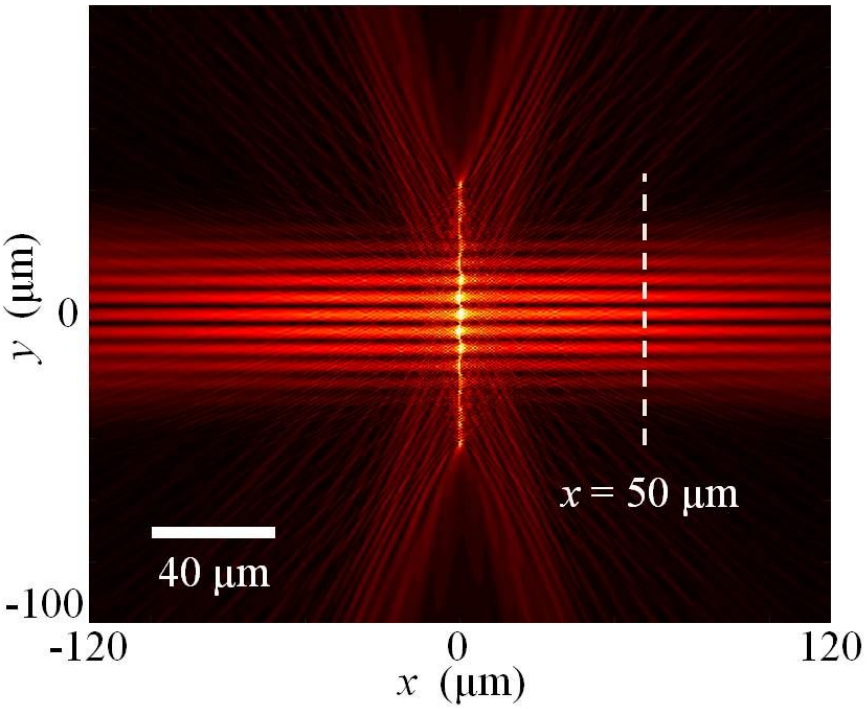

Figure 3.14 The intensity distribution of CGB calculated by Green dyadic method.

To analyze the quality of the generated CGB, the cross section of the simulated beams at x = 50 um was compared with the analytical calculations in Fig. 3.15. The blue line is the analytical calculation and the red line is the simulated CGB. There is good agreement between theory and simulation in terms of the locations of the peaks and dips of the beams in the range of y = [-10 μm, 10 μm]. Outside of this range, the simulated CGB shows a slightly higher intensity than that of theory. This difference is caused by the discrete nature of the design method which limits the resolution of the field

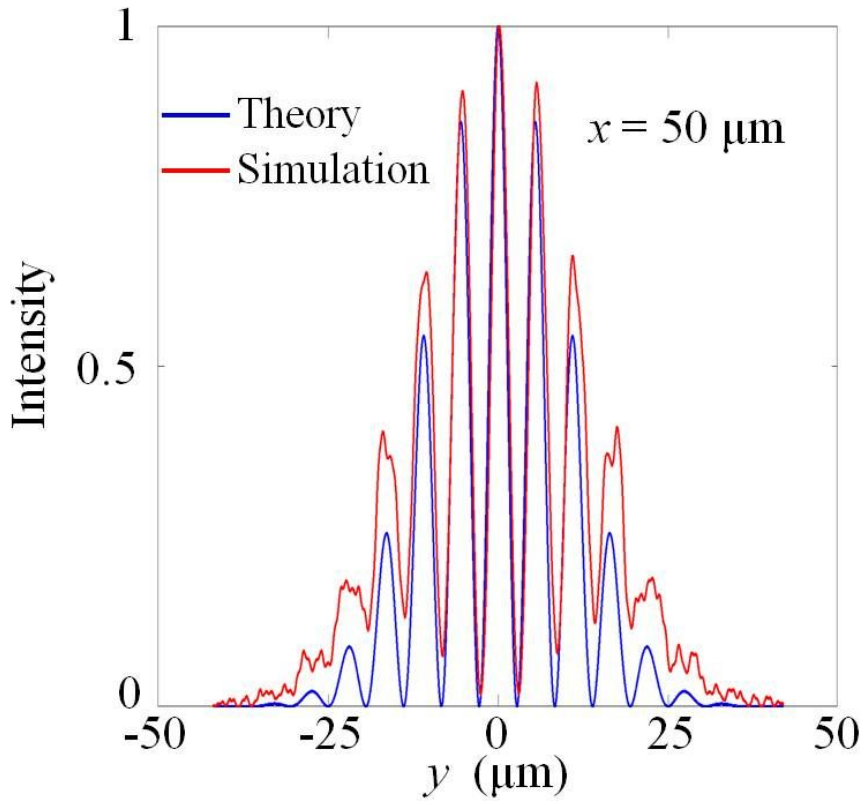

Figure 3.15 Cross-section of the simulated beams at x = 50 um compared with analytical calculations.

3.7 Complex Field Example: Plasmonic Airy Beam

3.7.1 Design of plasmonic Airy beams

Previous sections dealt with phase- and amplitude-only modulations of plasmonic field. In this section, I would like to manipulate the example which needs both of the amplitude and phase control together. For this purpose, I choose the appropriate example as a plasmonic Airy beam, which will be generated by similar procedure in the previous sections.

The envelope of the Airy packet represents an oscillating function with alternating positive maxima and negative minima. Therefore, the phase distribution of the Airy function shows alternating segments with values of 0 and π, which needs simultaneous design of amplitude and phase. The complex field profile of the Airy plasmon can be expressed as [34]

$$f(y) = Airy\left(\frac{y}{y_0}\right)\exp\left(a\frac{y}{y_0}\right). \tag{3.7}$$

The function *Airy* is an Airy function defined in [34], y_0 is a half width of main lobe, and a is a parameter defining exponential apodization of the Airy plasmon profile.

Following the same procedure as previous sections, I designed the tilted angles of double-lined nanoslit arrays. The locations of unit cells are shown in Figs. 3.16(a) and 3.16(b) for amplitude and phase, respectively. The sampling range is from y = -25 μm to y = 0 μm. The number of unit cells is 76 which determine the period of unit cells as 333 nm. I determined the slit dimension as 300 nm × 80 nm. In this section, I select the polarization as

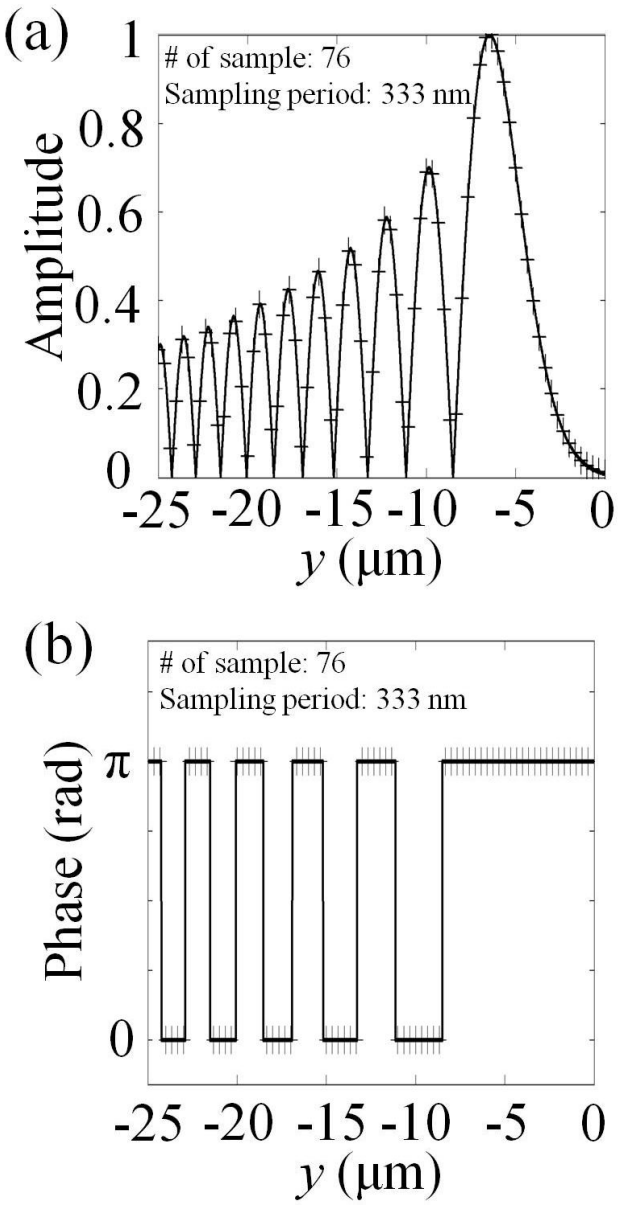

Figure 3.16 Airy complex field profile expressed as Eq. (2.7) for (a) amplitude and (b) phase. The locations of unit cells are also marked as '+'.

RCP. Similar to the case of previous example, I determined appropriate tilted angles, θ_L and θ_R along y-axis from the diagram shown in Fig. 3.4(b). It is noteworthy that there is a degree of freedom for determining tilted angles. Nevertheless, I numerically confirmed that SPP fields generated from these different sets of tilted angles make the identical intensity profile of Airy plasmon.

3.7.2 Simulation and experiment result

I provide the simulation and experimental result in Figs. 3.17(a) and 3.17(b), respectively. Blue dashed line is the main lobe trajectory of target Airy plasmon which can be expressed as [33]

$$y = \frac{x^2}{4k_{SPP}{}^2 y_0{}^3}, \tag{2.8}$$

where k_{SPP} is the wavenumber of SPP mode. I set the other geometrical parameters of Airy plasmon as y_0 = 1500 nm and a = 0.05. The calculated beam trajectory is in good agreement with the simulation result although it has limited unit cells range and discrete diffraction elements. Experimental result shows some deviations from the blue dashed curves showing diffraction of beam along +x-axis. Similar to previous example, I suppose that these deviations come from imperfect fabrication of nanoslit arrays and slightly oblique incidence of light.

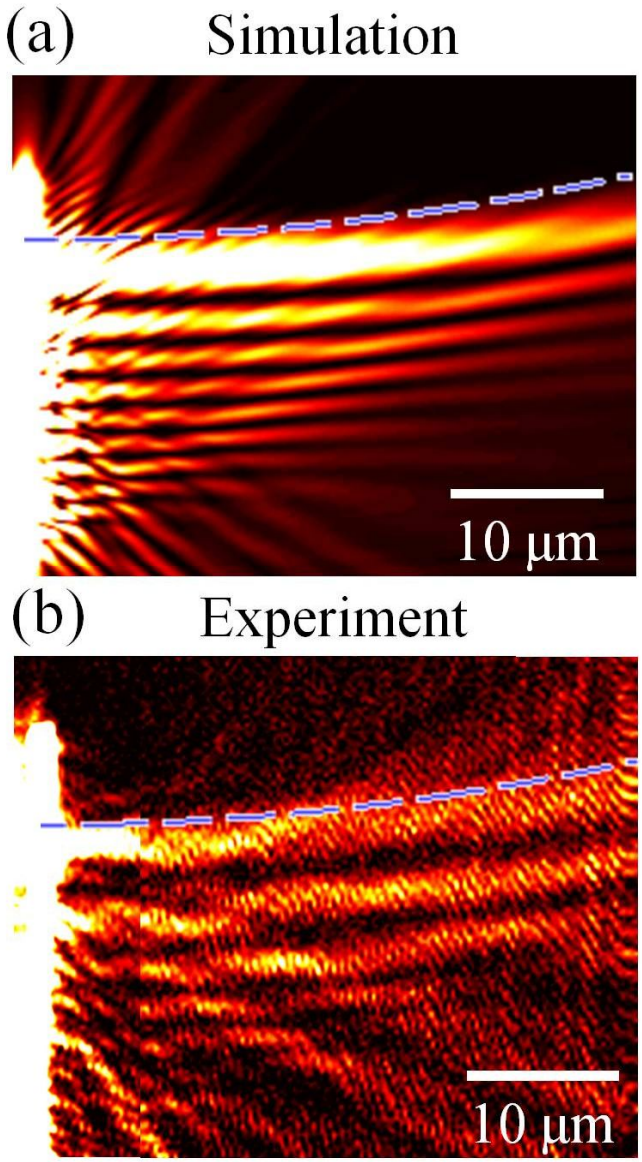

Figure 3.17 Results of plasmonic Airy beam generation in (a) numerical simulation and (b) NSOM measurement. Blue dashed curves are the main lobe trajectory of target Airy plasmon expressed as Eq. (3.8).

3.7.3 Degree of freedom for selecting the nanoslit angle

In designing the Airy beam profile, there are infinite ways for selecting sets of nanoslit angles from the complex unit circle. Because the Airy beam example only needs a continuously changing amplitude profile in the range of [0, 1], and discrete two phase values having the phase difference of π, the region required for expressing Airy beam can be any line cuts of a complex unit circle including the origin of the circle. The lines (A), (B) and (C) shown in Fig. 3.18 are some examples of different line cuts. By selecting tilted angles of nanoslit pairs from the different sets extracted from line (A), (B), and (C), it is possible to generate the Airy plasmon profiles shown in Figs. 3.19(a), 3.19(b), and 3.19(c), respectively. It is clearly shown that all of Airy beams have nearly identical shape even though they are formed by different sets of pairs of nanoslits.

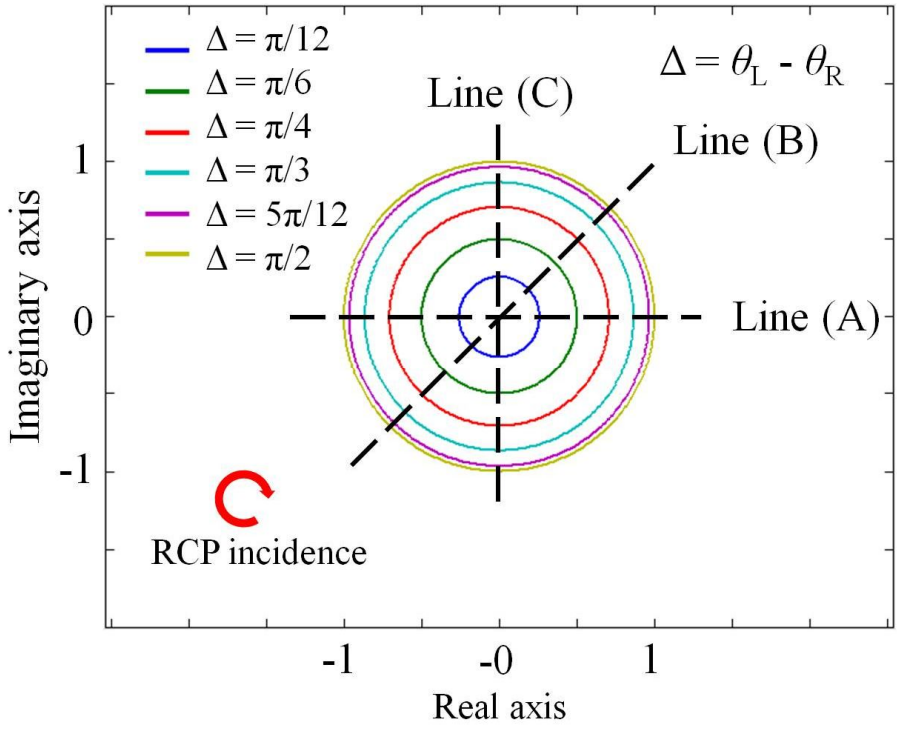

Figure 3.18 The range of complex field modulation is plotted when θ_R is changed from 0 to π for RCP. Lines (A), (B), and (C) represent various ways of designing Airy plasmon patterns.

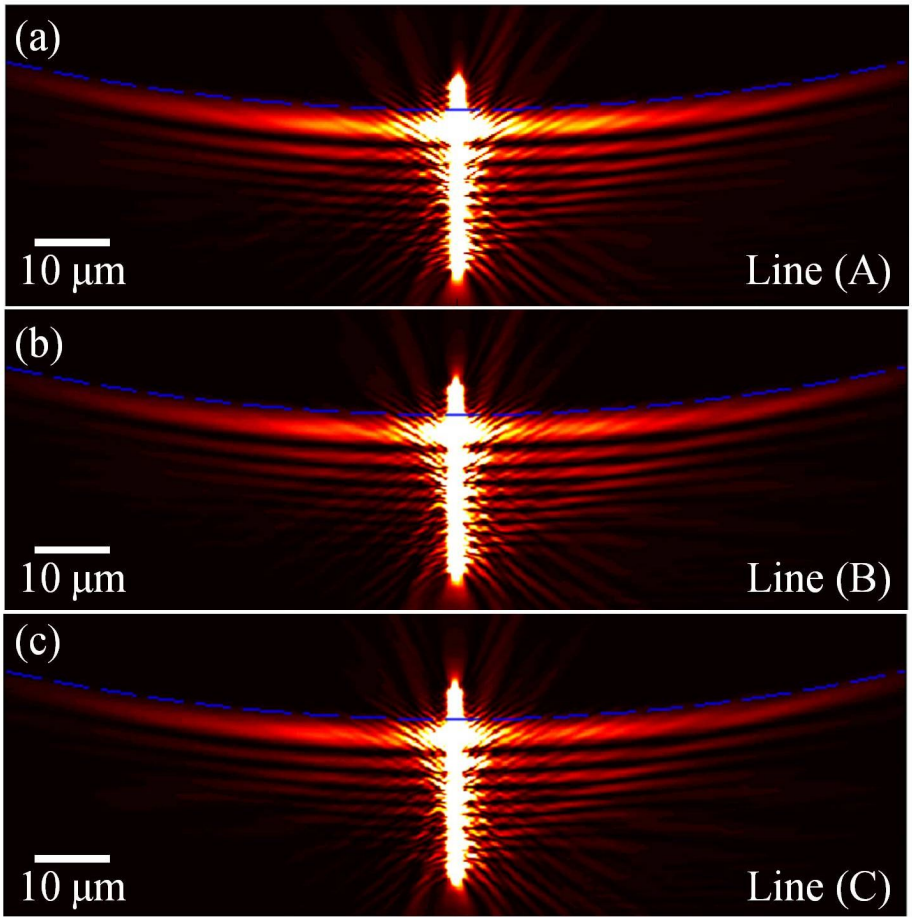

Figure 3.19 Numerical simulation results for the designed Airy plamons with (a) line (A), (b) line (B), and (c) line (C). Blue dashed curves are the main lobe trajectories of the target Airy plasmon patterns.

3.8 Steering of plasmonic complex beams based on oblique incident light

Throughout previous sections, I assumed that the direction of incident light is normal to the sample. However, it would be advisable to check the influence of the oblique incident light because the experimental setup can occasionally have an improper alignment. This situation is plotted in Fig. 3.20. For convenience, I analyzed the obliquely incident waves into two representative directions: The cases of the incident wave vector of the plane wave laid on the *z*-*x* plane (oblique incidence 1) and *y*-*z* plane (oblique incidence 2), respectively.

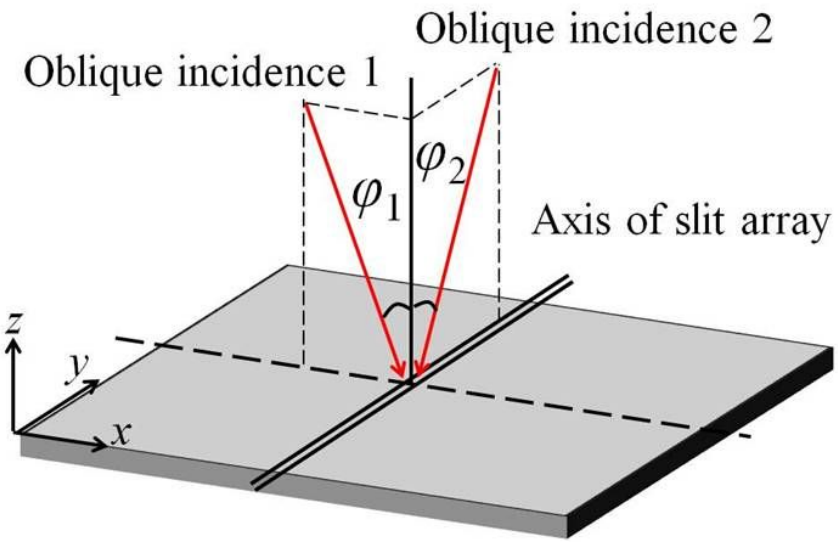

Figure 3.20 The configuration of the system used for checking the influence of the incident angle. The incident wave vector of the plane wave is laid on the *z*-*x* plane with oblique angle φ_1 or *y*-*z* plane with oblique angle φ_2.

Figure 3.21(a) shows the field distribution of the structure designed for the caustic curve $y_2 = a_2x^2$ when the incident wave vector is laid on the z-x plane ($\varphi_1 = 15^\circ$). Blue dashed curves are the target curves $y_2 = a_2x^2$. If the distance between two slit lines is given by D, the oblique angle φ_1 causes an additional phase difference $D\sin\varphi_1$ between two slit lines, which causes the disruption of symmetry and deviation from the target curve.

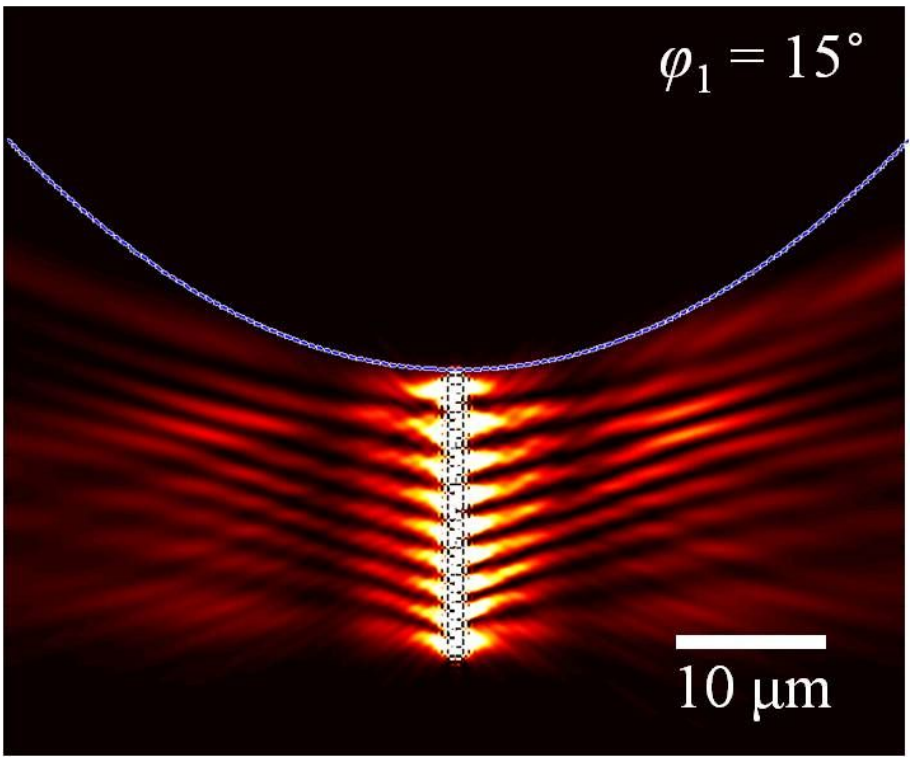

Figure 3.21 Field distribution on the structure designed for the caustic curve $y_2 = a_2x^2$ when the incident wave vector is laid on the z-x plane with an oblique angle of $\varphi_1 = 15^\circ$.

Figs. 3.22(a) and 3.22(b) show the field distribution on the structure designed for the caustic curve $y_2 = a_2x^2$ when the incident wave vector is laid on the y-x plane ($\varphi_2 = 10^\circ$ and $\varphi_2 = -10^\circ$, respectively). If the inter-slit period is given by P_y, the oblique angle φ_2 causes an additional phase difference $P_y\sin\varphi_2$ between the two adjacent slits. Because the phase profiles of the caustic curves are monotonic increasing functions of y, as shown in Fig. 3.23, these additional phase difference modifies the order n of analytical curve $y_2 = ax^n$. When the oblique angle is $\varphi_2 > 0$ (or $\varphi_2 < 0$), the order n of analytical curve increases (or decreases). This can be confirmed by the deviation shown in Figs. 3.22(a) and 3.22(b).

This observation can be used for steering plasmonic caustic beam. By controlling the oblique angle φ_2, the steering of plasmonic caustic beam can be facilitated. Fig 3.24 shows the example of caustic beam steering for analytical curve $y_2 = ax^2$.

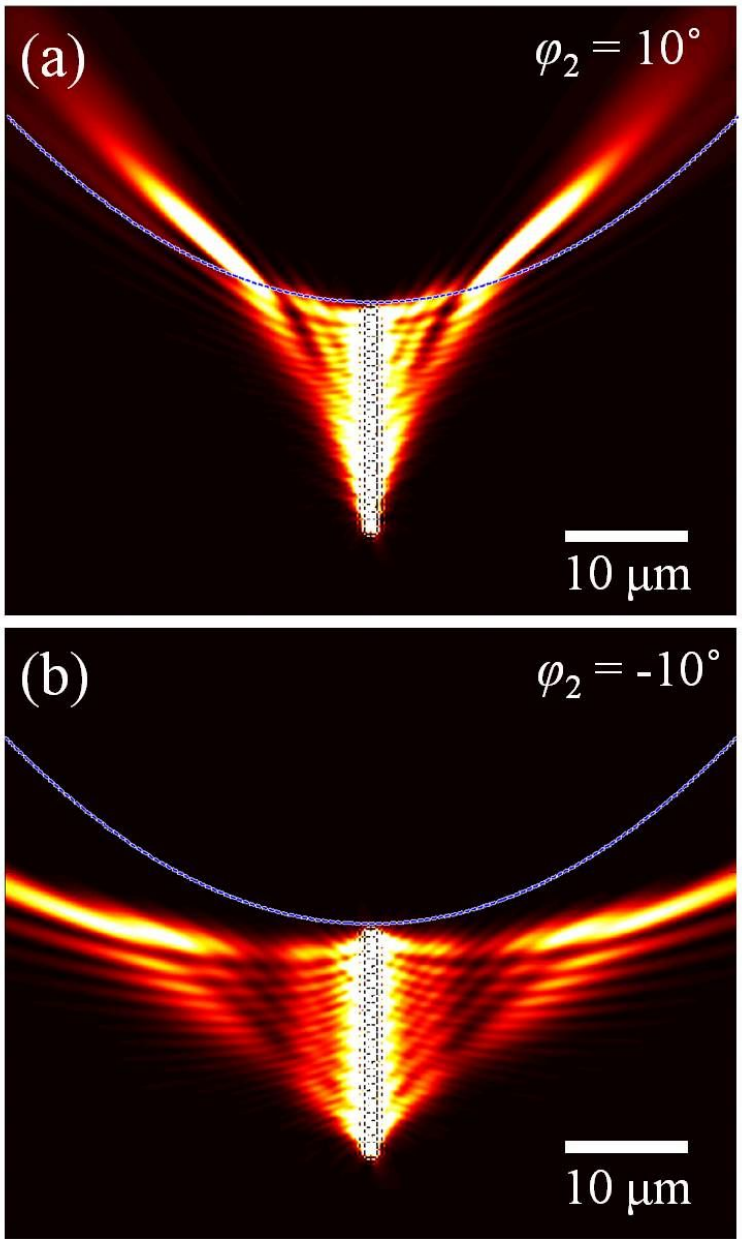

Figure 3.22 Field distributions on the structure designed for the caustic curve $y_2 = a_2x^2$ when the incident wave vector is laid on the y-x plane are plotted for (c) $\varphi_2 = 10^\circ$ and (d) $\varphi_2 = -10^\circ$.

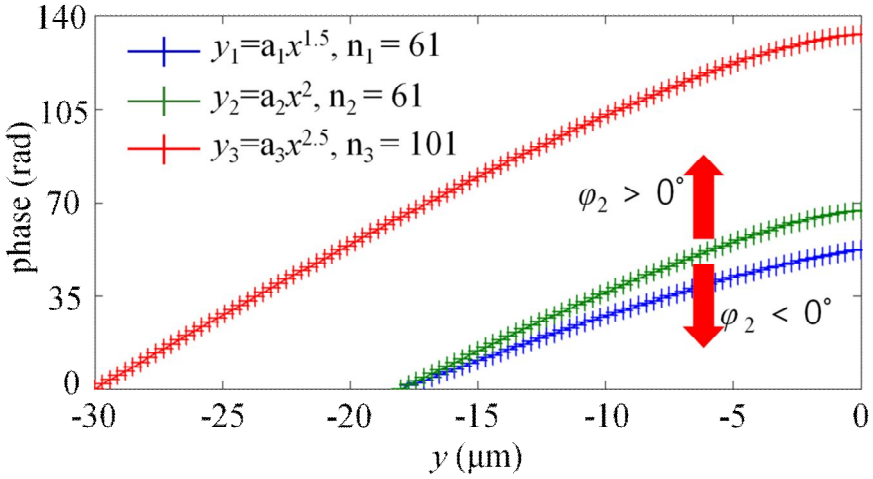

Figure 3.23 The phase profiles $\varphi(y)$ and their locations of unit cells for $y_1 = a_1x^{1.5}$, $y_2 = a_2x^2$, and $y_3 = a_3x^{2.5}$. The locations of unit cells are marked as '+'. By controlling oblique angle, modification of the order n of analytical curve $y_2 = ax^n$ is possible.

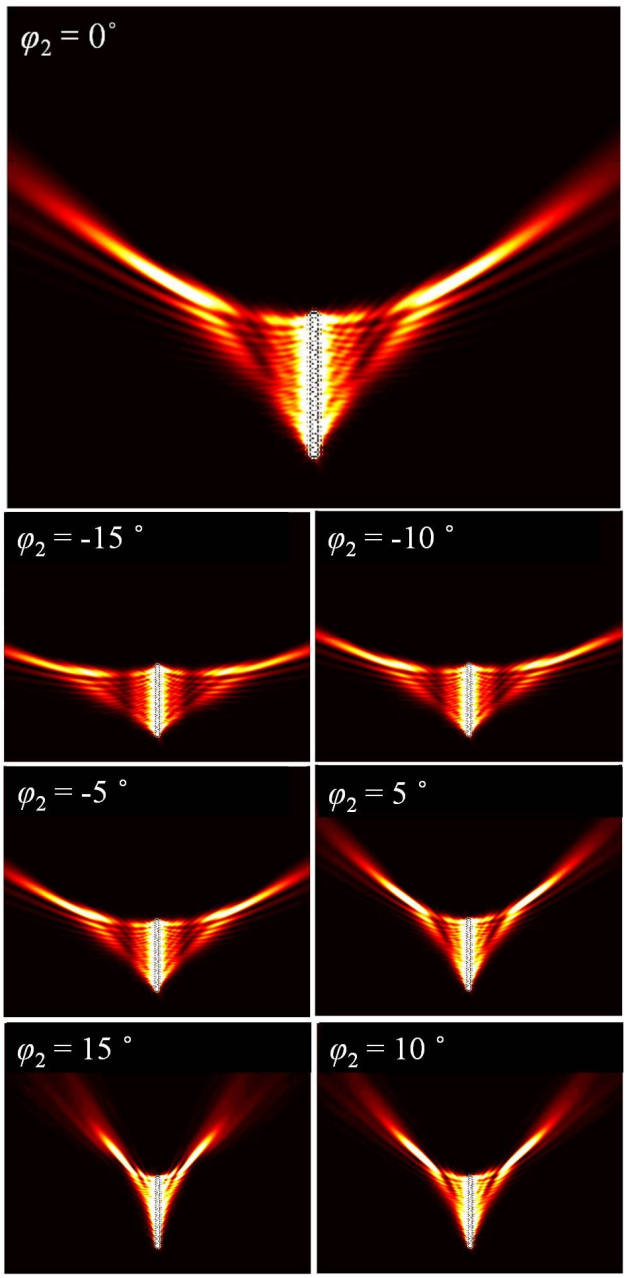

Figure 3.24 Field distributions on the structure designed for the caustic curve $y_2 = a_2x^2$ when the incident wave vector is laid on the y-x plane are plotted for various angle.

3.9 Conclusion

In conclusion, I proposed a novel method for generating a plasmonic complex field propagating with arbitrary curvatures by using double-lined distributed nanoslits. I initially set the desired plasmonic complex field profile (such as caustics or Airy beam profile) to be generated. Because the SPP sources are excited from the array of discrete nanoslits, it is necessary to substitute the complex field profile with unit cell. As a unit cell, two facing nanoslits are used for tuning both the amplitude and the phase of excited SPPs as a function of their tilted angles. After determining the appropriate dimension of the nanoslit and the unit cell period, the tilted angles are determined according to the type of circular polarization. Finally, I obtained the appropriate shape of the nanoslit array for plasmonic complex field generation. As long as the restricted slit size is realistic in fabrication, it is possible to generate an arbitrary plasmonic complex field with the proposed workflow. For verification of the proposed design rule, I experimentally demonstrated some plasmonic caustic curves, Airy plasmons, and cosine-Gaussian beams. The calculated and experimental results of beam trajectory are in good agreement with the simulation result although they have limited unit cell range and discrete diffraction elements. I expect that the proposed method of designing plasmonic complex field generation can be employed to excite various types of non-diffracting surface waves. Moreover, my results could be used for potential applications in integrated optics, plasmonic beam shaping, and next-generation holography.

Chapter 4 Metasurface for generation and steering of Airy beams

4.1 Introduction

In 1978, Berry and Balazs first predicted the non-speading wave packet from the Schrödinger equation in quantum mechanics for a free particle [6]. This wave packet is a non-trivial solution of the Schrödinger equation by exploiting the formal analogy between the free-particle Schrödinger equation and the paraxial equation of diffraction. The remarkable features of this Airy packet are non-spreading, freely accelerating, and self-healing ability. In 2007, optical version of the Airy wave packet, called Airy beams, was investigated and observed experimentally by introducing finite-energy Airy beams [7, 62]. Although the generated beam is not ideal Airy packet, the beam still showed all the interesting characteristics of ideal Airy packet: non-diffraction, free-acceleration and self-healing.

Over the years, Airy waves were generated by various ways including spatial light modulator (SLM) [63-65], specially designed lens system [66, 67], nonlinear method [68-70], electron [71], plasma [72], liquid crystal [73], surface grating [74], and subwavelength slit arrays [75]. Some of these reports showed that the generated Airy beams can be actively controlled. For example, ballistic motion of Airy beams was controlled using SLM [33]. In addition, Polarization-controllable Airy beams using liquid crystal mask have also been proposed [76]. However, micro-size pixels of the SLM or liquid

crystal restrict the design of Airy beams because these require bulky optical system and limit the application for small-scale or integrated beam-shaping devices. Nonlinear generation and manipulation of Airy beams also suffers from long crystal length for making sufficient nonlinear effect.

Recently, bulky optical components have started to be replaced by ultrathin and planar elements called metasurface. A metasurface is often defined as an artificially designed two-dimensional structure which can be made of arrays of subwavelength scatterers. The scatterers of metasurface have a variety of forms such as nanoparticles, apertures, and slit inscribed on the metallic films. Being as thin as only a fraction of the wavelength, the metasurface can change the wavefront of light abruptly. Furthermore, the size of unit cell in metasurface is much less than the wavelength which is important difference between metasurfaces and conventional optical devices using SLM or liquid crystal. Several metasurfaces were introduced which can modify the wavefront of light by altering its phase, amplitude and polarization in a desired manner [77-79].

In this context, metasurfaces may open new ways to generate and control Airy beams for compact, integrated optical systems. Recently, multifunctional optical beam shapers based on plasmonic metasurfaces were introduced [78]. Local polarization and wavelength selectivity of metasurfaces were combined with methods of computer-generated holograms for phase and amplitude modulation. This method successfully demonstrated switching between one-dimensional Airy and Gaussian beams, Hermite-Gaussian beams of different orders, and two-dimensional Airy and Bessel beams. Very recently, Second-harmonic Airy beams with tailored

beam profiles using nonlinear metasurfaces were introduced [80]. By tuning both the phase and the amplitude of quadratic nonlinear coefficient locally using computer-generated holograms, nonlinear beam shaping was facilitated.

In this paper, a novel method for generating and steering of Airy beams based on linear optical metasurface is proposed. To accomplish this, I used split ring resonators (SRRs) aperture arrays in which each SRR has its own tilted angle. The amplitude and phase of Airy beam profile can be substituted with unit cells and tailored by tuning only the tilted angles of the SRRs. Furthermore, the metasurface has a multi-frequency characteristic in optical regime. This facilitates steering of Airy beams by tuning the wavelength of incident light because the trajectory of Airy beams is a parabolic curve whose curvature is dependent on the wavelength. In comparison to previous approaches for generating and controlling Airy beams, my design method shows many important merits – ultrathin subwavelength pixel size for compact system, multi frequency characteristic, simple design strategy, and linear optical devices, which means that this method is more energy efficient than nonlinear metasurface method. To the best of my knowledge, it is the first realization of Airy beams having both multi-frequncy and compact (main lobe: ~ 2μm) characteristics.

4.2 Split ring resonator (SRR) based metarsurface for generation of Airy beam

4.2.1 Characteristics of unit cell based on split ring resonator shaped aperture

A schematic diagram of the proposed unit cell for generation of Airy beam is shown in Fig. 4.1. Au film with thickness t is deposited on the glass substrate. SRR pattern is inscribed on the Ag layer with tilted angle θ about x-axis. The subwavelength periods of this unit cell are P_x and P_y along x and y direction, respectively.

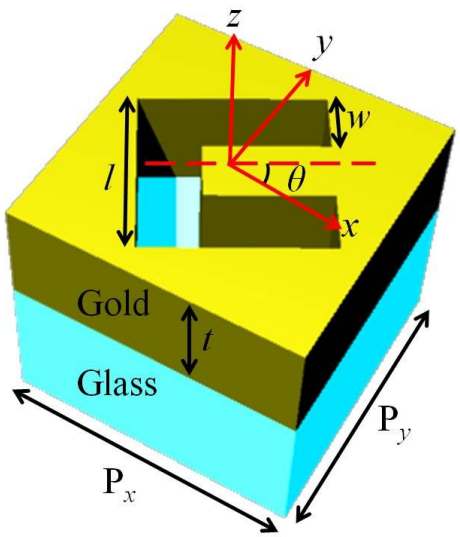

Figure 4.1 Schematics diagram of the proposed unit cell for generation of Airy beam.

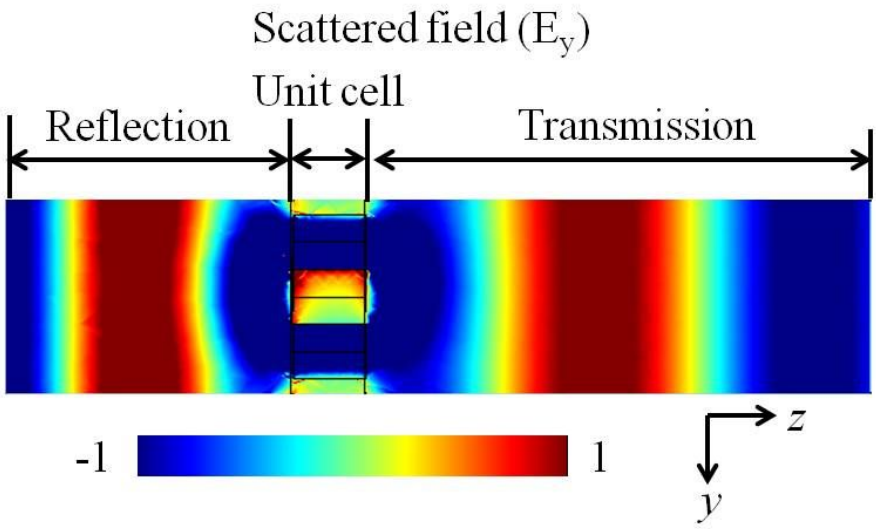

Figure 4.2 Electric field distribution (E_y) when *x*-polarized plane wave is backside illuminated.

When *x*-polarized plane wave is backside illuminated onto an SRR aperture arrays which have same tilted angle θ, the wavefront of transmitted *y*-polarized light is quasi-plane wave as shown in Fig. 4.2. In addition, its absolute amplitude and phase profiles can be tuned by the tilted angle θ of SRR apertures. In Figs. 4.3 and 4.4, changes in the relative amplitude and phase of the transmitted *y*-polarized light are plotted at 5μm away from the top of SRR aperture. The periods ($P_x = P_y$ = 400 nm), thickness of Au film (t = 150 nm), width and diameter of SRR aperture (w = 80 nm and l = 240 nm) are carefully chosen for experimental consideration. In Fig. 4.3, blue curves are normalized amplitude profiles of the four amplitude profiles with λ = 800 nm, λ = 900 nm, λ = 1000 nm and λ = 1100 nm which coincide with each other. These blue curves can be approximated as $\sin(2\theta)$. In Fig. 4.4, the phase profile shows two segments with values near 0 and near π. The

deviations from the exact 0 and π get larger as the wavelength gets shorter. In engineering perspective, however, we could approximate the two segments as values exact 0 and π because the maximum deviation is below 10%.

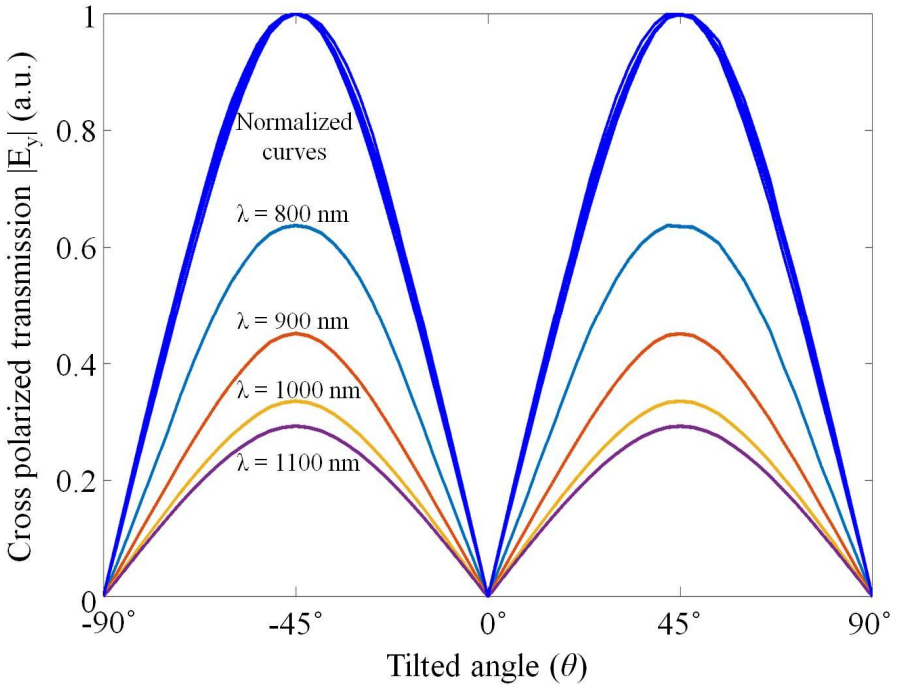

Figure 4.3 Relative amplitude of the transmitted *y*-polarized light at 5μm away from the top of SRR aperture.

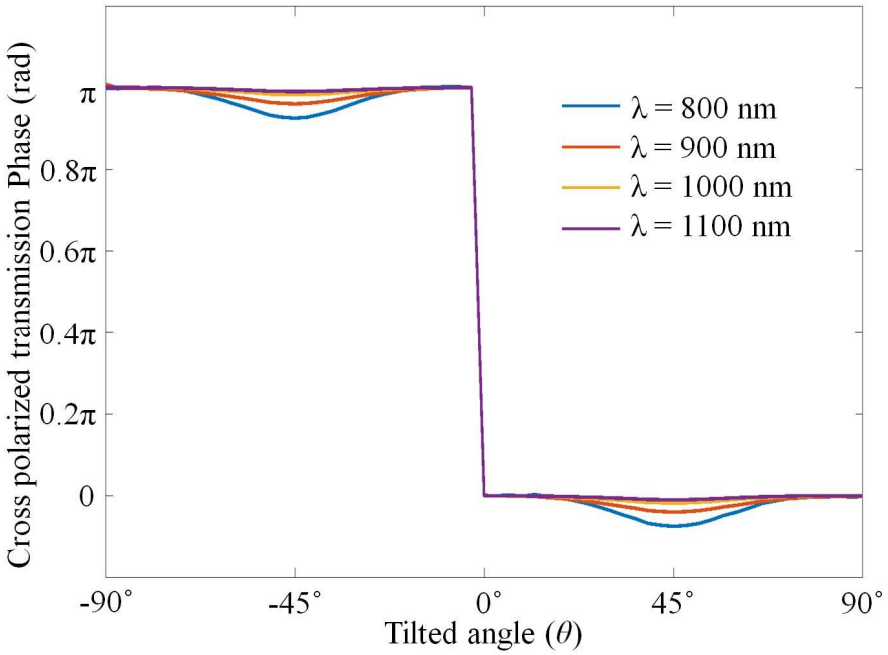

Figure 4.4 Phase of the transmitted *y*-polarized light at 5μm away from the top of SRR aperture.

In Figs. 4.5(a)-(d), *y*-polarized electric field distributions are shown 20 nm above the SRR aperture at selected tilted angles θ. At $\theta = 0^\circ$, an anti-symmetric mode about axis of SRR is generated. Because this anti-symmetric mode is canceled out in far-field region, this explains the dark state at $\theta = 0^\circ$ in Fig. 4.3. At $\theta = 90^\circ$, another anti-symmetric mode is generated which explains the dark state at $\theta = 90^\circ$ in the same way at $\theta = 0^\circ$. At the intermediate state like Figs. 4.5(c) and 4.5(d), these two anti-symmetric modes simultaneously contribute to the electric field distributions which break anti-symmetric distribution of electric field. Because this tendency is robust in the wavelength range of our interest (from $\lambda = 800$ nm to $\lambda = 1100$ nm), the proposed metasurface can be used in multi-frequency

design.

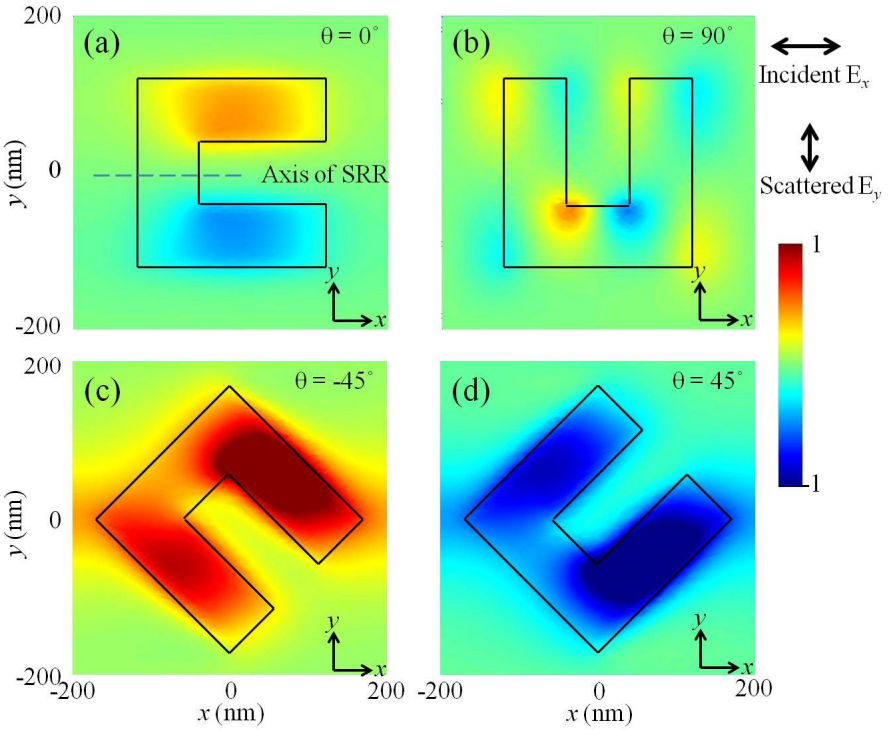

Figure 4.5 *y*-polarized electric field distributions at 20 nm above the SRR aperture for (a) $\theta = 0^{\circ}$, (b) $\theta = 90^{\circ}$, (c) $\theta = -45^{\circ}$, (d) $\theta = 45^{\circ}$.

4.2.2 Characteristics of unit cell based on split ring resonator shape antennas

In Fig 4.6, complementary structure of the unit cell in Fig 4.2 is plotted. The parameters of this structure are the same as the parameters in Fig 4.2. Amplitude and phase profiles of complementary antenna structure can be explained in similar ways with V- , C-shaped antennas [64-66].

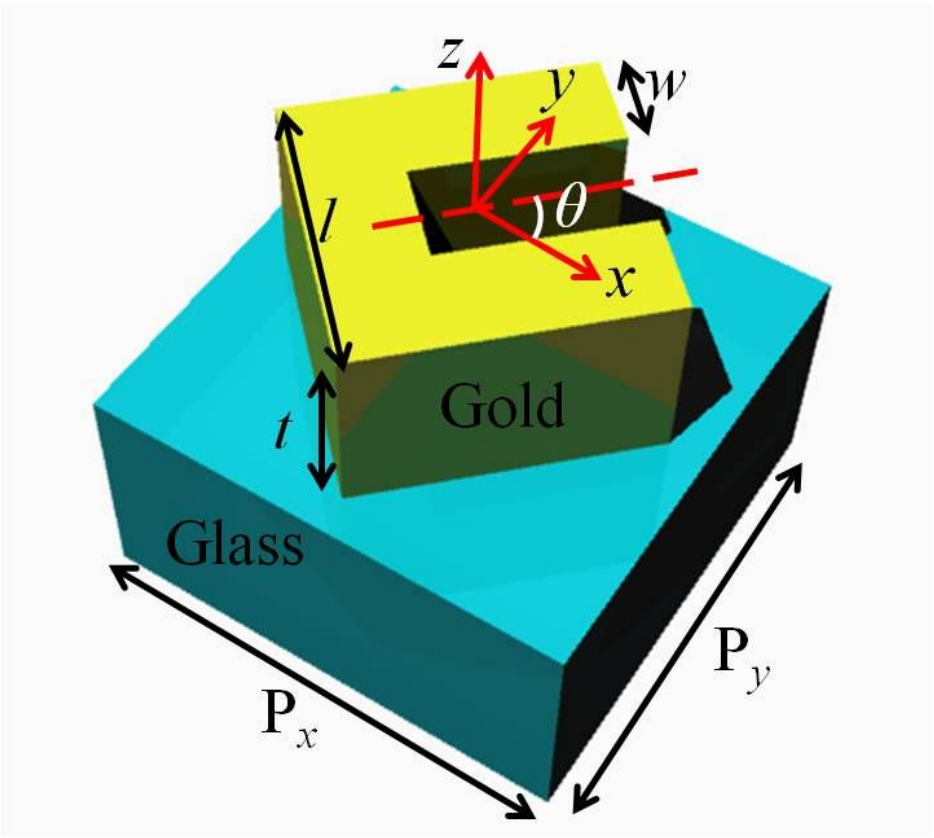

Figure 4.6 Schematics diagram of split ring resonator shaped antennas

By Babinet principle, relative amplitude and phase profiles of the transmitted *y*-polarized light of this antennas show similar profiles with Fig 3.3.

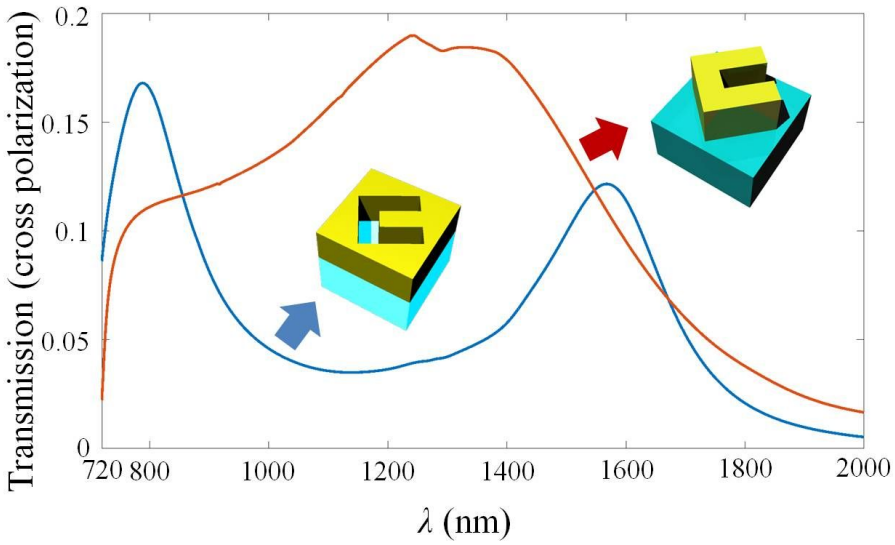

Figure 4.7 Comparison of power efficiency between split ring resonator aperture and antenna

In Fig. 4.7, comparison of power efficiency between split ring resonator aperture and antenna is shown. Power efficiency was calculated by setting tilted angle $\theta = 45^{\circ}$ at which the cross polarized transmission is maximum. In wavelength range from 720 nm to 850 nm, the power efficiency of aperture is greater than antenna. In wavelength range from 850 nm to 1500nm, the power efficiency of antenna is greater than aperture.

4.3 Design of metasurface for generation of Airy beams

I now describe the method of designing metasurface for generating Airy beams. The profile of (1+1)D Airy beam can be expressed as

$$f(x) = Airy\left(\frac{x}{x_0}\right)\exp\left(a\frac{x}{x_0}\right) \tag{4.1}$$

The function *Airy* is an Airy function defined in [20], x_0 is a half width of main lobe, and a is a parameter to obtain Airy beam with finite power. The envelope of the Airy packet represents an oscillating function with alternating positive maxima and negative minima. Therefore, the phase distribution of the Airy function shows alternating segments with values of 0 and π. Proposed unit cell in the previous section can encode the Airy beam profile by sampling Eq. (4.1) with constant unit cell period. Because Eq. (4.1) is one-dimensional equation related with x, the tilted angles of sampled unit cell along y-direction at the same x is identical. Fig. 4.8 shows the Airy beam profile and its locations of unit cells. At some selected locations, apertures with specific tilted angles are plotted.

The parameters of Eq. (4.1) was selected as x_0 = 1200 nm, a = 0.05. The unit cells range is from -20 μm to 4 μm. The number of unit cells is 61, which determines the period of unit cells as 400 nm.

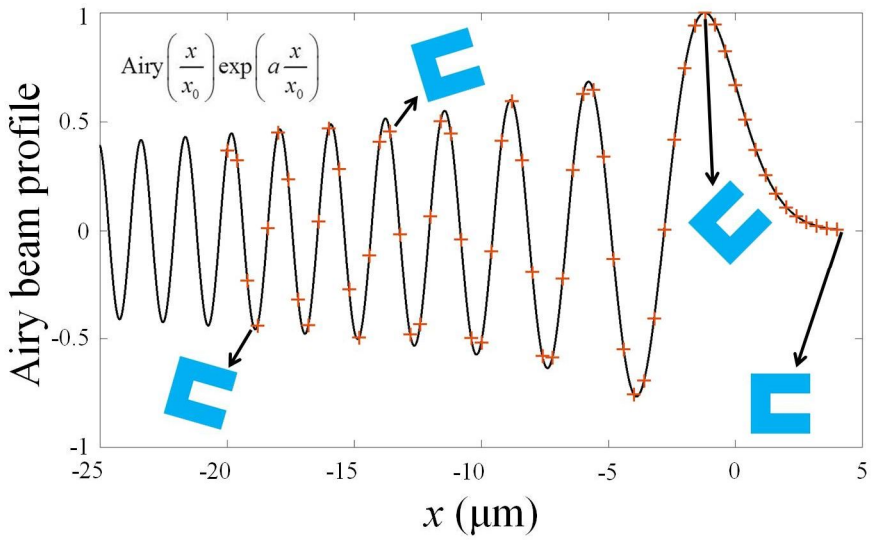

Figure 4.8 (1+1)D Airy beam profile. The locations of unit cells are marked as '+'. At some selected unit cells, apertures with specific tilted angles are plotted.

There are various points to be considered in designing metasurface. First of all, unit cell period P_x and P_y must be shorter than the operating wavelength to avoid unwanted generation of multiple beams. Second, the lower limit of the unit cell period is determined by the resolution limit in fabrication although shorter period of unit cell guarantees more accurate results. Attachment of neighboring two apertures is another point to consider.

After determining the appropriate dimension of the SRR aperture and the unit cell period with the abovementioned criteria, tilted angles are determined by using Fig. 4.3. Finally, the appropriate shape of the SRR aperture array for Airy beam generation is obtained. As long as the restricted aperture size is realistic in fabrication, it is possible to generate Airy beams with the proposed workflow.

4.4 Compact and multi-frequency Generation of Airy beams

4.4.1 Simulation of (1+1)D Airy beams

To verify the validity of the aforementioned design process, I provide some simulations. To simulate the intensity distribution of the generated (1+1)D Airy beams, I employed a commercial simulation tool (CST Microwave Studio 2016). The numerical simulations for free space wavelength λ = 750 nm, 800 nm, 900 nm, and 1000 nm are presented in Fig. 4.9. Simulation results of the four curves are in good agreement with the blue dashed curves, which are the targeted trajectory of main lobe. Small deviations from the blue dashed curves in the figures are evident as the Airy beams propagate along z axis. I conclude that this small mismatch originates from the finite number of unit cells which causes the Airy lobes to spread out. This restricts the range of the SPP curves that exactly follow the blue dashed curves. In order to accelerate the Airy lobe more rapidly, it is necessary to substitute the Airy profiles with unit cells on more broad range. In Fig. 4.9(a), the side lobes show interference in medium range. This is due to deviation from ideal Airy beam profile as shown in Fig. 4.4 which generates multiple beams at unit cells.

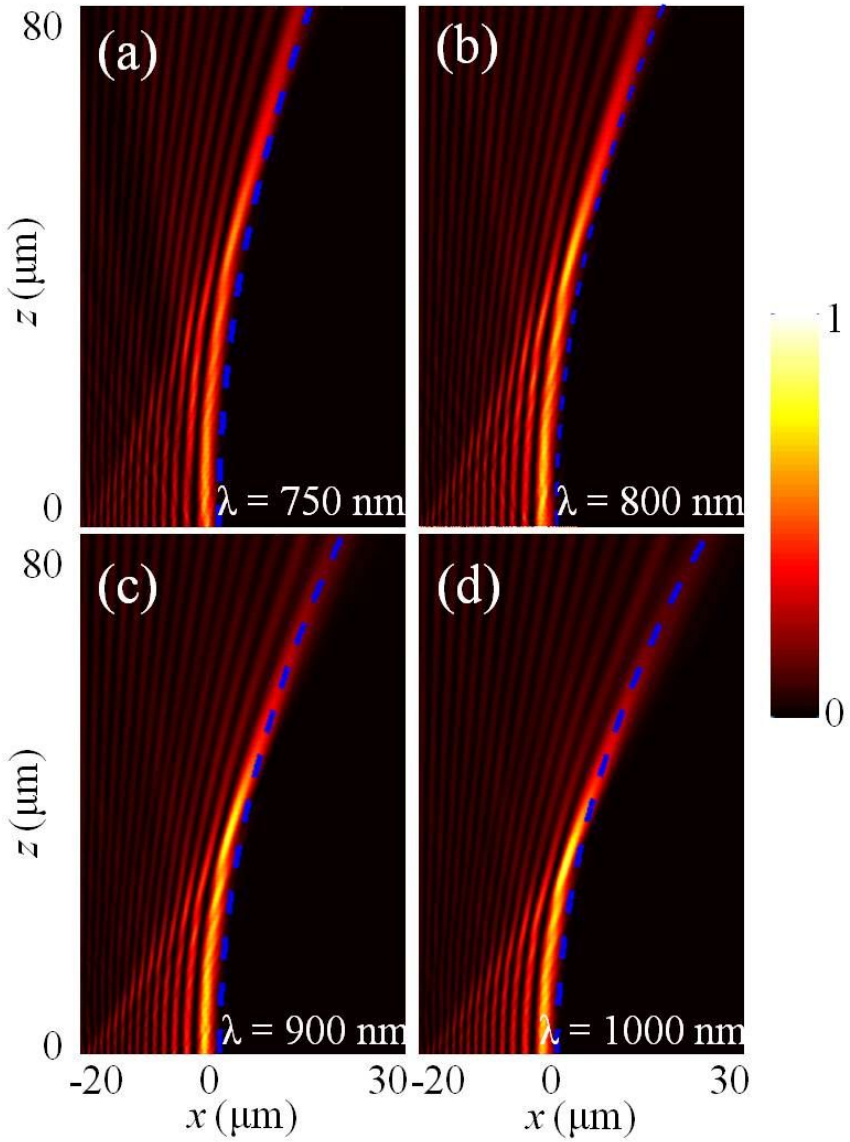

Figure 4.9 Numerical simulations results for the (1+1)D Airy beams for the free space wavelength (a) λ = 750 nm, (b) λ = 800 nm, (c) λ =900 nm, and (d) λ =1000 nm. Blue dashed curves are the targeted trajectories of main lobe.

4.4.2 Experiment of (2+1)D Airy beams

To verify the simulation results, I provide some experimental results. The design procedure is identical with that of (1+1)D Airy beams. The profile of (2+1)D Airy beams is as follows which is two dimensional version of Eq. 4.1.

$$f(x) = Airy\left(\frac{x}{x_0}\right) Airy\left(\frac{y}{y_0}\right) \exp\left(a\frac{x}{x_0}\right) \exp\left(a\frac{y}{y_0}\right), \qquad (4.2)$$

The parameters of Eq (4.2) were selected as x_0 = 1200 nm, y_0 = 1200 nm and a = 0.05. The unit cells range is from -14μm to 4μm for x and y direction. The number of unit cells is 46 by 46, which determines the period of unit cells as 400 nm along x and y direction.

For sample fabrication, an Au layer with a thickness of 150 nm was evaporated on a fused silica wafer (MUHAN, MHS-1800). Then SRR patterns were inscribed on the Au layer using a focused ion beam (FIB) (FEI, Helios 650). Fig. 4.10 shows the field-enhanced scanning electron microscope (FE-SEM) images of the fabricated sample for generation of Airy beams. According to the right-side image with a higher magnification, it is possible to confirm that the size of the fabricated SRR pattern is smaller than the unit cell period. The sample was then illuminated from the bottom by a laser with the free-space wavelength of λ = 800 nm and λ = 980 nm. The incident light on the sample was polarized with x-direction. Transmitted light was cross-polarized with y-direction and the generated Airy beam intensity distribution was measured by CCD camera. The experimental setup is shown in Fig. 4.11.

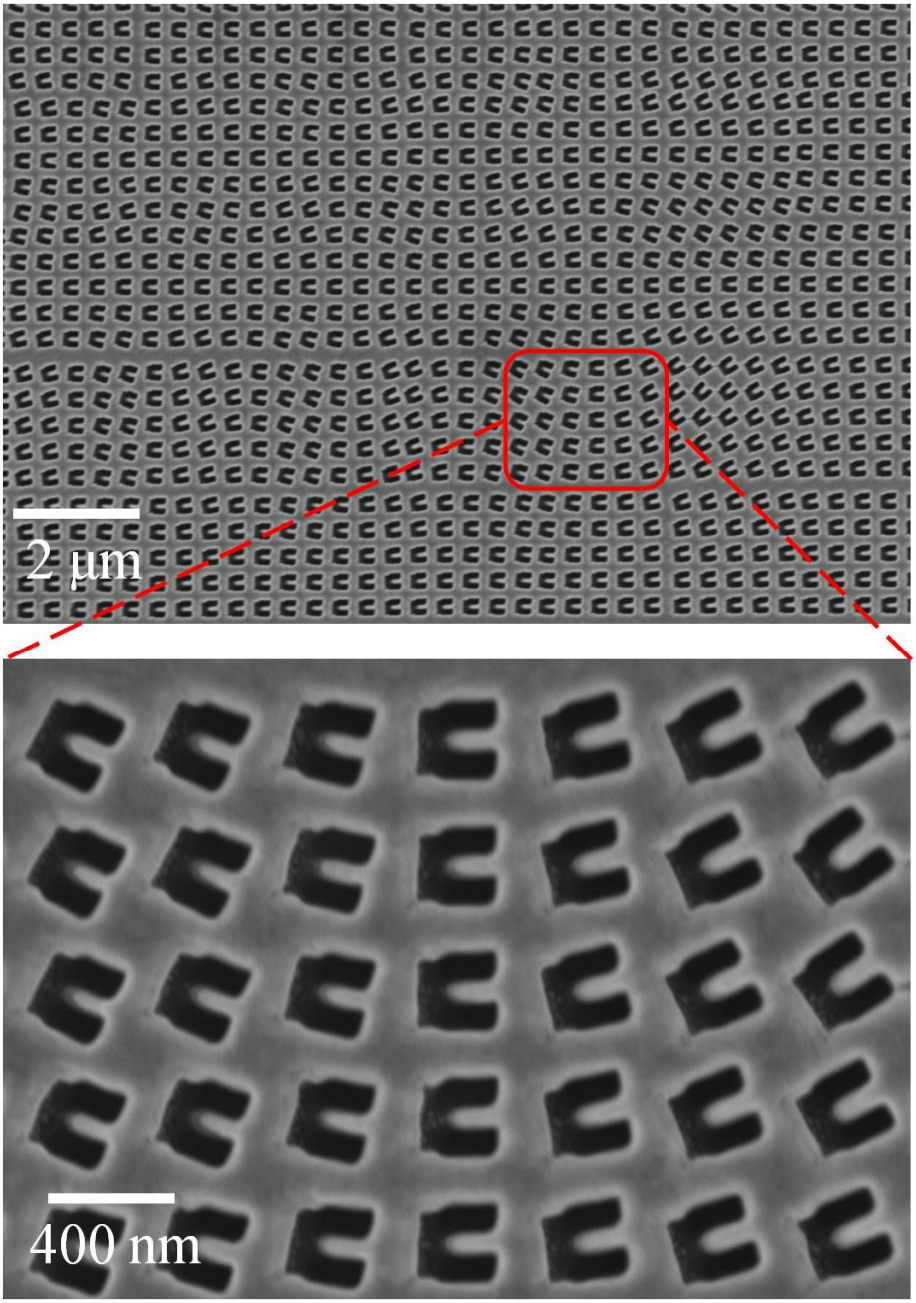

Figure 4.10 FE-SEM images of fabricated sample for (2+1) Airy beam generation.

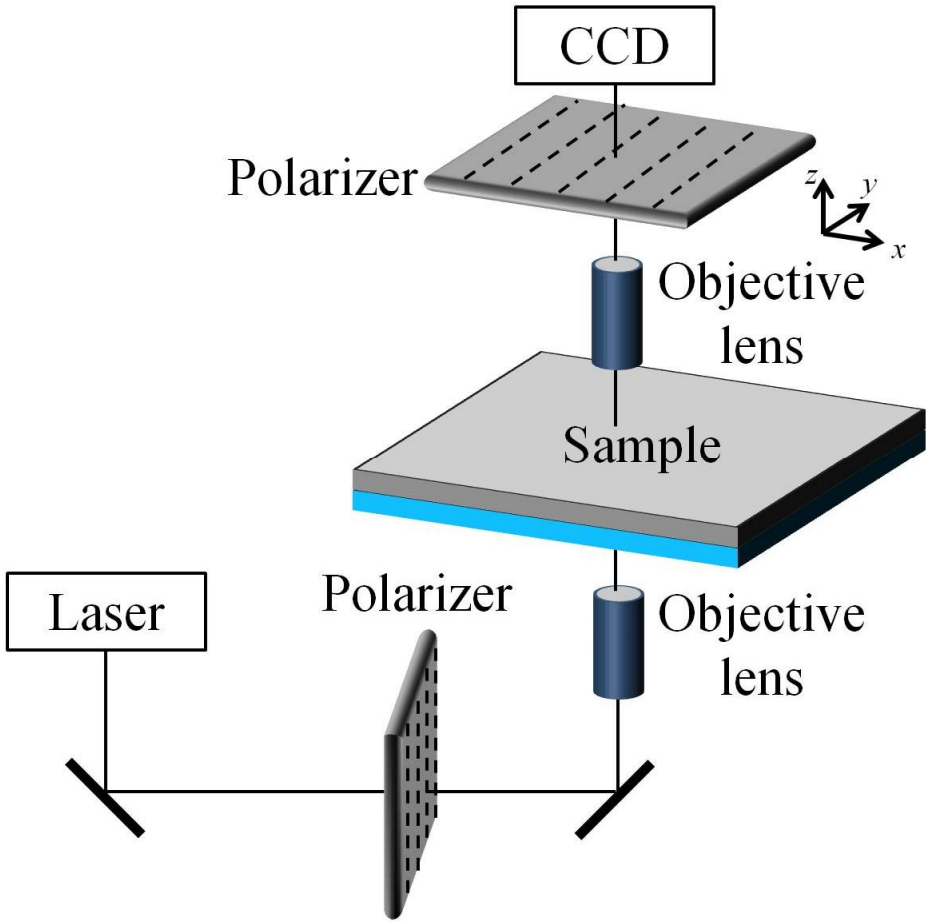

Figure 4.11 Experimental setup for cross polarized light measurement.

The experimental results for the (2+1)D Airy beams are presented in Figs. 4.12 and 4.13. In these figures, analytical and experimental results for z= 0 μm, z= 40 μm, z= 80 μm, and z= 120 μm, at wavelength λ = 800 nm and λ = 976 nm were plotted. Experimental results show some deviation from analytical results. I believe that the finite numerical aperture of the objective lens in the experimental setup might play a role that causes the intensity of the incident light and the incidence angle to be non-uniform. Deflections of

Airy beam with respect to z of analytic and experimental results are slightly different from the analytical results. This can be explained as coming from the finite number of samples which restrict the Airy beams from deflection.

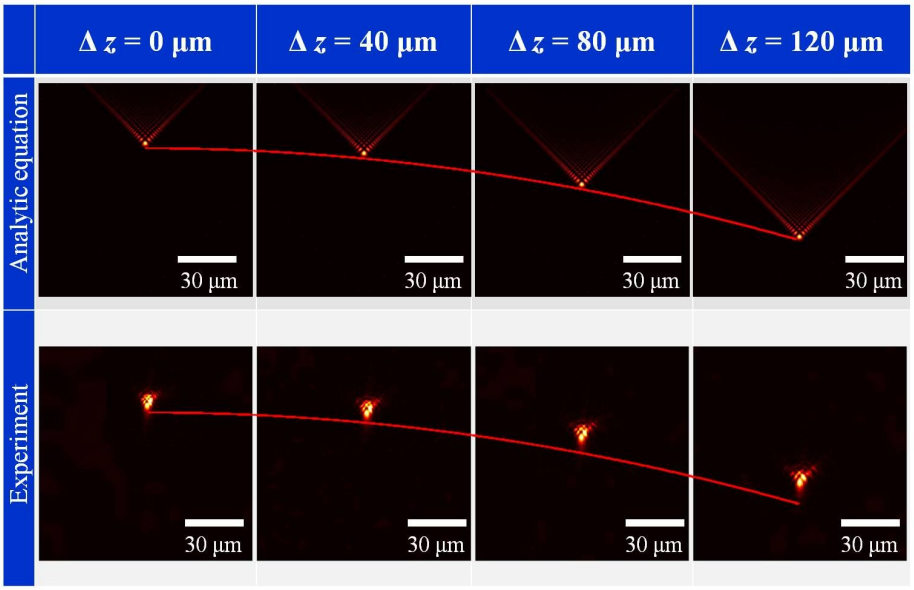

Figure 4.12 Analytical and experimental results for z= 0 μm, *z*= 40 μm, *z*= 80 μm, and *z*= 120 μm at wavelength λ = 800 nm.

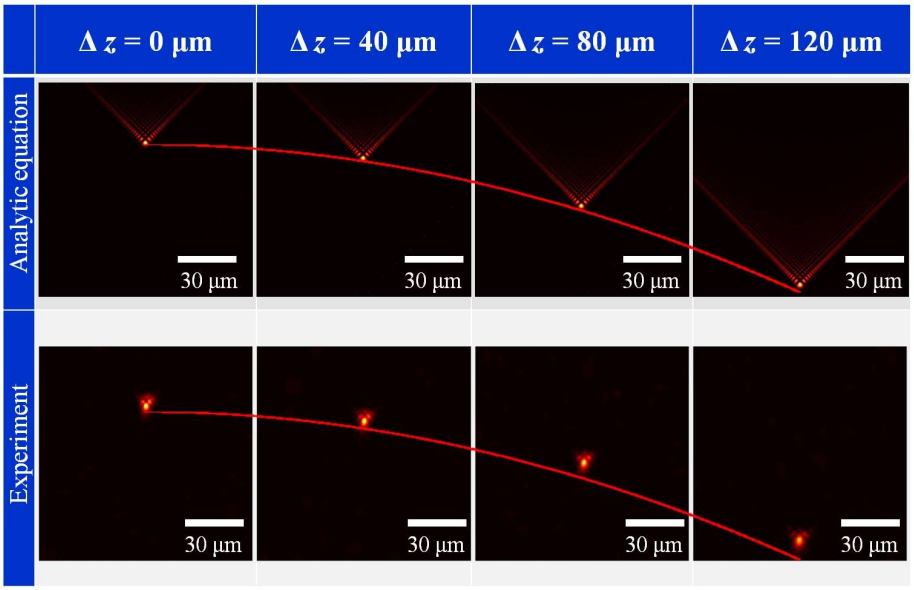

Figure 4.13 Analytical and experimental results for *z*= 0 μm, *z*= 40 μm, *z*= 80 μm, and *z*= 120 μm at wavelength λ = 976 nm.

4.5 Conclusion

In conclusion, a novel method for generating and steering of Airy beams based on linear optical metasurface was proposed. To accomplish this, I used split ring resonator (SRR) aperture arrays in which each SRR has its own tilted angle. The envelope of the Airy packet represents an oscillating function with alternating positive maxima and negative minima. Therefore, the phase distribution of the Airy function shows alternating segments with values of 0 and π. Proposed unit cell can encode the Airy beam profile by substituting the profile with tilted angles of unit cells. Experimental results show some deviation from analytical results. I believe that the finite numerical aperture of the objective lens in the experimental setup might play a role that causes the intensity of the incident light and the incidence angle to be non-uniform. Deflections of Airy beam with respect to z of analytic and experimental results are slightly different from the analytical results. This can be explained as coming from the finite number of samples which restrict the Airy beams from deflection. In comparison to previous approaches for generating and controlling Airy beams, my design method showed many important merits – ultrathin subwavelength pixel size for compact system, broadband characteristic, simple design strategy, and linear optical devices, which means that this method is more energy efficient than nonlinear metasurface method. I expect that our proposed method of designing Airy beam generation can be employed to excite various types of Airy beams.

Chapter 5 Summary

This dissertation proposed methods for active generation and control of two types of optical beams: optical beam in free space and SPPs. I generated and controlled two types of optical beams: Airy beams and optical collimated beaming. For optical collimated beaming, a novel mechanism for active directional beaming by mechanical actuation of double-sided plasmonic surface gratings was proposed. Two diffracted beams with the same direction of radiation, and formed by diffraction of the leftward and rightward surface plasmon waves are spatially superposed by the surface gratings. This results in collimated directional beaming. It was shown that the radiation angle increases monotonically with the refractive indices of the double-sided gratings. The direction of the diffracted beam can be controlled by lifting the surface gratings to balance the effective refractive indices of the left- and right-gratings. Finally, it was shown that the asymmetric mechanical actuation of optimally designed plasmonic surface gratings surrounding a subwavelength metal slit can produce a steerable off-axis beaming effect. The controllability of the beam direction will provide an opportunity to develop novel active plasmonic devices and systems.

For SPPs type, I proposed a novel method for generating a plasmonic complex field propagating with arbitrary curvatures by using double-lined distributed nanoslits. I initially set the desired plasmonic complex field

profile (such as caustics or Airy beam profile) to be generated. Because the SPP sources are excited from the array of discrete nanoslits, it is necessary to substitute the complex field profile with unit cell. As a unit cell, two facing nanoslits are used for tuning both the amplitude and the phase of excited SPPs as a function of their tilted angles. After determining the appropriate dimension of the nanoslit and the unit cell period, the tilted angles are determined according to the type of circular polarization. Finally, I obtained the appropriate shape of the nanoslit array for plasmonic complex field generation. As long as the restricted slit size is realistic in fabrication, it is possible to generate an arbitrary plasmonic complex field with the proposed workflow. For verification of the proposed design rule, I experimentally demonstrated some plasmonic caustic curves, Airy plasmons, and cosine-Gaussian beams. The calculated and experimental results of beam trajectory are in good agreement with the simulation result although they have limited unit cell range and discrete diffraction elements.

For Airy beams, a novel method for generating and steering of Airy beams based on linear optical metasurface was proposed. To accomplish this, I used split ring resonators (SRRs) aperture arrays in which each SRR has its own tilted angle. The envelope of the Airy packet represents an oscillating function with alternating positive maxima and negative minima. Therefore, the phase distribution of the Airy function shows alternating segments with values of 0 and π. Proposed unit cell can encode the Airy beam profile by substituting the profile with tilted angles of unit cells. Experimental results show some deviation from analytical results. I believe that the finite numerical aperture of the objective lens in the experimental setup might play

a role that causes the intensity of the incident light and the incidence angle to be non-uniform. Deflections of Airy beam with respect to z of analytic and experimental results are slightly different from the analytical results. This can be explained as coming from the finite number of samples, which restricts the Airy beams from deflection. In comparison to previous approaches for generating and controlling Airy beams, the proposed design method showed many important merits – ultrathin subwavelength pixel size for compact system, multi-frequency characteristic, simple design strategy, and linear optical devices, which means that this method is more energy efficient than nonlinear metasurface method.

Bibliography

1. J. Baumgartl, M. Mazilu, and K. Dholakia, “Optically mediated particle clearing using Airy wavepackets,” Nat. Photonics **2**(11), 675–678, (2008).
2. F. O. Fahrbach, P. Simon, and A. Rohrbach, “Microscopy with self-reconstructing beams,” Nat. Photon. **4**, 780-785, (2010).
3. B. Lee, “Three-dimensional displays, past and present,” Phys. Today **66**, 36-41 (2013).
4. R. F. Oulton, V. J. Sorger, T. Zentgraf, R.-M. Ma, C. Gladden, L. Dai, G. Bartal, and X. Zhang, “Plasmon lasers at deep subwavelength scale,” Nature. **461**, 629-632, (2009).
5. E.-Y. Song, H. Kim, W. Y. Choi, and B. Lee, "Active directional beaming by mechanical actuation of double-sided plasmonic surface gratings," Optics Letters, **38**(19), 3827-3829, (2013).
6. M. V. Berry and N. L. Balazs, “Nonspreading wave packets,” Am. J. Phys. **47**(3), 264–267 (1979).
7. G. A. Siviloglou and D. N. Christodoulides, “Accelerating finite energy Airy beams,” Opt. Lett. **32**(8), 979–981, (2007).
8. J. Durnin, “Exact solutions for nondiffracting beams. I. The scalar theory,” J. Opt. Soc. Am. A **4**(4), 651–654, (1987).
9. J. Durnin, J. J. Miceli, Jr., and J. H. Eberly, “Diffraction-free beams,” Phys. Rev. Lett. **58**(15), 1499–1501, (1987).
10. J. Durnin, J. J. Miceli, Jr., and J. H. Eberly, “Comparison of Bessel and

Gaussian beams," Opt. Lett. **13**(2), 79– 80, (1988).

11. D. McGloin and K. Dholakia, "Bessel beams: diffraction in a new light," Contemp. Phys. **46**(1), 15–28, (2005).
12. J. C. Gutiérrez-Vega, M. D. Iturbe-Castillo, G. A. Ramírez, E. Tepichín, R. M. Rodríguez-Dagnino, S. Chávez-Cerda, and G. H. C. New, "Experimental demonstration of optical Mathieu beams," Opt. Commun. **195**, 35–40, (2001).
13. J. Gutiérrez-Vega, M. Iturbe-Castillo, and S. Cháavez-Cerda, "Alternative formulation for invariant optical fields: Mathieu beams." Opt. Lett. **25**, 1493–1495, (2000).
14. B. Lee, S. Kim, H. Kim, and Y. Lim, "The use of plasmonics in light beaming and focusing," Progress in Quantum Electronics, **34**(2), 47-87, (2010).
15. T. Vettenburg, H. I. Dalgarno, J. Nylk, C. C-Lladó, D. E. K. Ferrier, T. Čižmár, F. J. G.-Moore, and K. Dholakia, "Light-sheet microscopy using an Airy beam," Nature Methods, 11(5), 541-547, (2014).
16. Y. C. Jun, K. C. Huang, and M. L. Brongersma, "Plasmonic beaming and active control over fluorescent emission," Nat. Commun. doi: 10.1038/ncomms1286, (2011)
17. H. Aouani, O. Mahboub, E. Devaux, H. Rigneault, T. W. Ebbesen, and J. Wenger, "Plasmonic Antennas for Directional Sorting of Fluorescence Emission," Nano Lett. 11(6), 2400-2406, (2011).
18. Y. Lee, K. Hoshino, A. Alu, and X. Zhang, "Tunable directive radiation of surface-plasmon diffraction gratings," Opt. Express **21**, 2748, (2013).
19. S. Reichelt, R. Häussler, G. Fütterer, N. Leister, H. Kato, N. Usukura,

and Y. Kanbayashi, “Full-range, complex spatial light modulator for real-time holography,” Opt. Lett. **37**, 1955, (2012).

20. T. Kosako, Y. Kadoya, and H. F. Hofmann, “Directional control of light by a nano-optical Yagi–Uda antenna,” Nat. Photonics **4**, 312, (2010).
21. H. J. Lezec, A. Degiron, E. Devaux, R. A. Linke, L. Martin-Moreno, F. J. Garcia-Vidal, and T. W. Ebbesen, “Beaming light from a subwavelength aperture,” Science **297**, 820, (2002).
22. E. Ozbay, “Plasmonics: Merging Photonics and Electronics at Nanoscale Dimensions,” Science **311**, 189, (2006).
23. H. Kim, J. Park, and B. Lee, “Tunable directional beaming from subwavelength metal slits with metal–dielectric composite surface gratings,” Opt. Lett. **34**, 2569, (2009).
24. J.-Y. Ou, E. Plum, J. Zhang, and N. I. Zheludev, “An electromechanically reconfigurable plasmonic metamaterial operating in the near-infrared,” Nat. Nanotechnol. **8**, 252, (2013).
25. K. V. Acoleyen, J. Roels, T. Claes, D. V. Thourhout, and R. Baets, in IEEE International Conference on Group IV Photonics (2011), p. 371.
26. Y. S. Hwang, J. Kim, K.-Y. Kim, “An improved design formula for the plasmonic directional beaming of light,” IEEE Photon. Technol. Lett. **26,** 2051-2054, (2014).
27. J. Park, H. Kim, I.-M. Lee, S. Kim, J. Jung, and B. Lee, “Resonant tunneling of surface plasmon polariton in the plasmonic nano-cavity,” Opt. Express **16**, 16903, (2008).
28. E. S. Hung and S. D. Senturia, “Extending the travel range of analog-tuned electrostatic actuators,” J. Microelectromech. Syst. **8**, 497, (1999).

29. S. Maier, *Plasmonics: Fundamentals and Applications*, Springer, (2007).
30. O. Brzobohatý, M. Šiler, J. Trojek, L. Chvátal, V. Karásek, A. Paták, Z. Pokorná, F. Mika, and P. Zemánek, "Three-dimensional optical trapping of a plasmonic nanoparticle using low numerical aperture optical tweezers," Sci. Rep. **5**, 8106, (2015).
31. M. L. Juan, M. Righini, and R. Quidant, "Plasmon nano-optical tweezers,",Nature Photon. **5**, 349–356, (2011).
32. I. Epstein and A. Arie, "Arbitrary bending plasmonic light waves," Phys. Rev. Lett. **112**, 023903, (2014).
33. P. Zhang, S. Wang, Y. Liu, X. Yin, C. Lu, Z. Chen, and X. Zhang, "Plasmonic Airy beams with dynamically controlled trajectories," Opt. Lett. **36**, 3191–3193, (2011).
34. A. Minovich, A. E. Klein, N. Janunts, T. Pertsch, D. N. Neshev, and Y. S. Kivshar, "Generation and near-field imaging of Airy surface plasmons," Phys. Rev. Lett. **107**, 116802, (2011).
35. P. Genevet, J. Lin, M. A. Kats, and F. Capasso, "Holographic detection of the orbital angular momentum of light with plasmonic photodiodes," Nature Commun. **3**, 1278, (2012).
36. D. Wintz, P. Genevet, A. Ambrosio, A Woolf, and F. Capasso, "Holographic metalens for switchable focusing of surface lasmons," Nano Lett. **15**, 3585–3589, (2015).
37. A. E. Cetin, A. F. Coskun, B. C. Galarreta, M. Huang, D. Herman, A. Ozcan, and H. Altug, "Handheld high-throughput plasmonic biosensor using computational on-chip imaging," Light Sci. Appl. **3**, e122 (2014).
38. A. G. Brolo, "Plasmonics for future biosensors," Nature Photon. **6**, 709–

713, (2012).

39. H. Kim, J. Park, S.-W. Cho, S.-Y. Lee, M. Kang, and B. Lee, "Synthesis and dynamic switching of surface plasmon vortices with plasmonic vortex lens," Nano Lett. **10**, 529–536, (2010).
40. Z. Fang, Q. Peng, W. Song, F. Hao, J. Wang, P. Nordlander, and X. Zhu, "Plasmonic focusing in symmetry broken nanocorrals," Nano Lett. **11**, 893–897, (2011).
41. Y. Gorodetski, A. Niv, V. Kleiner, and E. Hasman, "Observation of the spin-based plasmonic effect in nanoscale structures," Phys. Rev. Lett. **101**, 043903, (2008).
42. W.-H. Lee, "Binary computer-generated holograms," Appl. Opt. **18**, 3661–3669, (1979).
43. I. Epstein and A. Arie, "Dynamic generation of plasmonic bottle-beams with controlled shape," Opt. Lett. **39**, 3165–3168, (2014).
44. I. Epstein, Y. Lilach, and A. Arie, "Shaping plasmonic light beams with near-field plasmonic holograms," J. Opt. Soc. Am. B **31**, 1642–1647, (2014).
45. P. A. Huidobro, M. L. Nesterov, L. Martín-Moreno, and F. J. García-Vidal, "Transformation optics for plasmonics," Nano Lett. **10**, 1985–1990, (2010).
46. G. D. Valle and S. Longhi, "Graded index surface-plasmon-polariton devices for subwavelength light management," Phys. Rev. B **82**, 153411, (2010).
47. T. Zentgraf, Y. Liu, M. H. Mikkelsen, J. Valentine, and X. Zhang, "Plasmonic Luneburg and Eaton lenses," Nature Nanotechnol. **6**, 151–

155, (2011).

48. A. B. Evlyukhin, S. I. Bozhevolnyi, A. L. Stepanov, and J. R. Krenn, "Splitting of a surface plasmon polariton beam by chains of nanoparticles," Appl. Phys. B **84**, 29–34, (2006).
49. A. Drezet, D. Koller, A. Hohenau, A. Leitner, F. R. Aussenegg, and J. R. Krenn, "Plasmonic crystal demultiplexer and multiports," Nano Lett. **7**, 1697–1700, (2007).
50. O. Avayu, I. Epstein, E. Eizner, and T. Ellenbogen, "Polarization controlled coupling and shaping of surface plasmon polaritons by nanoantenna arrays," Opt. Lett. **40**, 1520–1523, (2015).
51. J. Lin, J. Dellinger, P. Genevet, B. Cluzel, F. de Fornel, and F. Capasso, "Cosine-Gauss plasmon beam: a localized long-range nondiffracting surface wave," Phys. Rev. Lett. **109**, 093904, (2012).
52. N. Yu, and F. Capasso, "Flat optics with designer metasurfaces," Nature Mater. **13**, 139–150, (2014).
53. N. Yu, F. Aieta, P. Genevet, M. A. Kats, Z. Gaburro, and F. Capasso, "A broadband, background-free quarter-wave plate based on plasmonic metasurfaces," Nano Lett. **12**, 6328–6333, (2012).
54. S. Sun, Q. He, S. Xiao, Q. Xu, X. Li, and L. Zhou, "Gradient-index meta-surfaces as a bridge linking propagating waves and surface waves," Nature Mater. **11**, 426–431, (2012)..
55. J. Lin, J. P. B. Mueller, Q. Wang, G. Yuan, N. Antoniou, X.-C. Yuan, and F. Capasso, "Polarization-controlled tunable directional coupling of surface plasmon polaritons," Science **340**, 331–334, (2013).
56. S.-Y. Lee, K. Kim, S.-J. Kim, H. Park, K.-Y. Kim, and B. Lee,

"Plasmonic meta-slit: shaping and controlling near-field focus," Optica **2**, 6–13, (2015).

57. S.-Y. Lee, S.-J Kim, H. Kwon, and B. Lee, "Spin-direction control of high-order plasmonic vortex With double-ring distributed nanoslits," IEEE Photon. Technol. Lett. **27**, 705–708, (2015).
58. G. Spektor, A. David, B. Gjonaj, G. Bartal, and M. Orenstein, "Metafocusing by a metaspiral plasmonic lens," Nano Lett. **15**, 5739–5743, (2015).
59. S.-Y. Lee, K. Kim, G.-Y. Lee, and B. Lee, "Polarization-multiplexed plasmonic phase generation with distributed nanoslits," Opt. Expess. **23**, 15598–15607, (2015).
60. L. Froehly, F. Courvoisier, A. Mathis, M. Jacquot, L. Furfaro, R. Giust, P. A. Lacourt, and J. M. Dudley, "Arbitrary accelerating micron-scale caustic beams in two and three dimensions," Opt. Expess. **19**, 16455–16465, (2011).
61. J. Lin, J. Dellinger, P. Genevet, B. Cluzel, F. Fornel, and F. Capasso, "Cosine-Gauss Plasmon Beam: A Localized Long-Range Nondiffracting Surface Wave," Phys. Rev. Lett. **109**, 093904, (2012).
62. G. A. Siviloglou, J. Broky, A. Dogariu, and D. N. Christodoulides, "Observation of accelerating Airy beams," Phys. Rev. Lett. **99**(21), 213901, (2007).
63. G. A. Siviloglou, J. Broky, A. Dogariu, and D. N. Christodoulides, "Ballistic dynamics of Airy beams," Opt. Lett. **33**(3), 207–209, (2008).
64. Y. Hu, P. Zhang, C. Lou, S. Huang, J. Xu, and Z. Chen, "Optimal control of the ballistic motion of Airy beams," Opt. Lett. **35**(13), 2260–2262,

(2010).

65. J. Baumgartl, M. Mazilu, and K. Dholakia, “Optically mediated particle clearing using Airy wavepackets,” Nat. Photonics **2**(11), 675–678, (2008).
66. B. Yalizay, B. Soylu, and S. Akturk, “Optical element for generation of accelerating Airy beams,” J. Opt. Soc. Am, **27**(10), 2344-2346, (2010).
67. D. G. Papazoglou, S. Suntsov, D. Abdollahpour, and S. Tzortzakis, “Tunable intense Airy beams and tailored femtosecond laser filaments,” Phys. Rev. A, **81**, 061807(R) , (2010).
68. T. Ellenbogen, N. V.-Bloch, A. G.-Padowicz, and A. Arie, “Nonlinear generation and manipulation of Airy beams,” Nature Photon. **3**, 395–398, (2009).
69. D. Wei, Y. Yu, M. Cao, L. Zhang, F. Ye, W. Guo, S. Zhang, H. Gao, F. Li, “Generation of Airy beams by four-wave mixing in Rubidium vapor cell,” Opt. Lett., **39**, 4557-4559, (2014).
70. I. Dolev, T. Ellenbogen, N. Voloch, and A. Arie, “Control of free space propagation of Airy beams generated by quadratic nonlinear photonic crystals” Appl. Phys. Lett. **95**, 201112, (2009).
71. N. V.-Bloch, Y. Lereah, Y. Lilach, A. Gover, and A. Arie, “Generation of electron Airy beams,” Nature **494**, 331–335, (2013).
72. P. Polynkin, M. Kolesik, J. V. Moloney, G. A. Siviloglou, and D. N. Christodoulides, “Curved plasma channel generation using ultraintense Airy beams,” Science **324**, 229-232, (2009).
73. B. Y. Wei, P. Chen, W. Hu, W. Ji, L. Y. Zheng, S. J. Ge, Y. Ming, V. Chigrinov, and Y. Q. Lu, “Polarization-controllable Airy beams

generated via a photoaligned director-variant liquid crystal mask," Sci. Rep. **5**, 17484, (2015).

74. I. Dolev, I. Epstein, and A. Arie, "Surface-plasmon holographic beam shaping," Phys. Rev. Lett. **109**, 203903, (2012).
75. D. Choi, Y. Lim, I.-M. Lee, S. Roh, and B. Lee, "Airy beam excitation using a subwavelength metallic slit array," IEEE Photonics Technology Letters, **24**(16), 1440-1442, (2012).
76. Ori Avayu, Omri Eisenbach, Ran Ditcovski, and Tal Ellenbogen, "Optical metasurfaces for polarization-controlled beam shaping," Opt. Lett. **39**(13), 3892-3895 , (2014).
77. S. Keren-Zur, O. Avayu, L. Michaeli, and T. Ellenbogen, "Nonlinear Beam Shaping with Plasmonic Metasurfaces," ACS Photon. **3**, 117-123 , (2015).
78. X. Ni, N. K. Emani, A. V. Kildishev, A. Boltasseva, V. M. Shalaev, "Broadband light bending with plasmonic nanoantennas," Science, **335**, 427, (2012).
79. N. Yu, P. Genevet, M. A. Kats, F. Aieta, J. P. Tetienne, F. Capasso, Z. Gaburro, "Light Propagation with Phase Discontinuities: Generalized Laws of Reflection and Refraction," Science, **334**, 333-337, (2011).
80. L. Liu, X. Zhang, M. Kenney, X. Su, N. Xu, C. Ouyang, Y. Shi, J. Han, W. Zhang, and S. Zhang, "Broadband metasurfaces with simultaneous control of phase and amplitude," Adv. Mater. **26**(29), 5031–5036, (2014).

Appendix

Portions of the work discussed in this dissertation are also presented in the following publications:

[Chapter 3] E.-Y. Song, H. Kim, W. Y. Choi, and B. Lee, "Active directional beaming by mechanical actuation of double-sided plasmonic surface gratings," Optics Letters, vol. 38, no. 19, pp. 3827-3829, 2013.

[Chapter 5] E.-Y. Song, S.-Y Lee, J. Hong, K. Lee, Y. Lee, G.-Y Lee, and B. Lee, “Double-lined metasurface for plasmonic complex field generation,”, Laser & Photonics Review, vol. 10, no. 2, pp. 299-308, 2016.

In addition, the author published the paper about compex modulation:
E.-Y. Song, J. Cho, H. Kim, W. Y. Choi, and B. Lee, "Double bi-material cantilever structures for complex surface plasmon modulation," Optics Express, vol. 23, no. 5, pp. 5500-5507, 2015.

초 록

본 박사학위 논문에서는 금속 나노 구조에 기반하여 광학 빔을 형성시키거나 조종하는 방법들을 제안한다. 회절하지 않는 빔이나 큰 지향성을 가지는 빛을 능동적으로 형성하고 조종하는 방법에 대한 연구는 빛의 특정 부위의 세기를 조절할 필요가 있거나 빛의 방출특성을 조절할 필요가 있는 분야에서 큰 관심을 얻어왔다. 하지만 이러한 기능을 할 수 있는 능동 소자들은 많은 관심에 비해 큰 진전을 보이지 못했다. 특히 나노 스케일이나 마이크로 스케일에서는 한 픽셀에서 조차도 광학 빔을 능동적으로 형성시키고 조종할 수 있는 방법에 대해서는 아직까지도 많은 진전이 필요하다.

본 박사학위 논문에서 집중하고자 하는 광학 빔은 형태에 따라서 여러 종류로 나뉜다. 에어리 빔, 초면(caustic) 빔, 코사인 가우스 빔, 광 지향성 비밍(optical directional beaming)이 바로 그것이다. 특히, 앞의 세 종류의 빔은 표면 플라즈몬 폴라리톤의 형태로도 형성되고 조종될 것이다. 이러한 빔들을 능동적으로 제어하기 위해서 본 논문에서는 세가지 메커니즘을 제시한다: 사입사, 파장 변환, 기계적인 조작이 그 세가지 메커니즘이다.

우선, 금속 슬릿을 통과한 빛이 지향성을 가지도록 슬릿의 양쪽에 회절격자를 설계하고 그 구조를 바탕으로 지향성을 가지는 빛의 방향을 능동 조절할 수 있는 방법을 제시할 것이다. 이 방법은 회절격자를 띄워서 양 격자가 서로 반대 부호를 가지는 각도로 지향성 빛을 발생시키는 것이다. 회절격자가 떠있는 정도를

기계적으로 제어하면 광 지향성 빛의 방향을 능동적으로 제어 할 수 있다.

두번째로, 빛이 슬릿을 통과하여 나오는 표면 플라즈몬의 진폭과 위상을 모두 동시에 변조하는 방법을 제안한다. 이 방법은 11자 형태의 슬릿 배열구조를 이용한다. 단위 셀로서, 두개의 마주보는 나노슬릿이 각각 기울어진 각도에 따라 발생하는 표면 플라즈몬의 진폭과 위상을 변조시킬 수 있다. 이에 대해 자세한 설계 방법을 알아보고 전산모사와 실험 결과를 통해 검증한다.

마지막으로, 공간상에서 유한 파워를 지니는 에어리빔을 메타표면을 이용하여 발생시킨다. Split ring resonator 형태의 나노개구 어레이에서 각 단위 셀의 기울어진 각도를 조절함으로써 에어리 빔을 발생시킬 수 있다. 특히 이러한 구조를 이용했을 경우 발생한 에어리빔은 크기가 마이크로미터 단위로 매우 작고 파장에 대해서도 광대역이다. 제안된 메타표면 구조를 검증하기 위해서 전산모사와 실험 결과를 제시할 것이다.

주요어: 광학 빔, 비회절 빔, 광 비밍, 메타표면, 플라즈모닉 빔, 에어리 빔, 초면 빔.

학 번: 2012-30939